POLITECNICO
DI TORINO

Dipartimento di Ingegneria Meccanica e Aerospaziale

Corso di Laurea Magistrale in Ingegneria Biomedica

INVESTIGATING THE PHYSIOLOGICAL SIGNIFICANCE OF HELICAL FLOW IN PERSONALIZED COMPUTATIONAL HEMODYNAMIC MODELS OF HUMAN CORONARY ARTERIES

Relatore:
Prof. Morbiducci Umberto

Correlatori:
Prof. Gallo Diego
Ing. De Nisco Giuseppe

Candidato:
MARZOCCHI Nicolò
Matricola: 252443

Anno Accademico 2019-2020

Contents

Figures Index

Tables Index

Abstract

Previous findings suggested that helical flow (HF) (1) protects from atherosclerosis by suppressing flow disturbances in main human arteries (such as thoracic aorta and carotid bifurcation), and (2) is inversely associated with atherosclerosis at the early stage. In addition, very recent studies involving swine-specific computational hemodynamic models highlighted that (1) counter-rotating HF patterns naturally develop in pig's coronary arteries and are negatively associated with descriptors of disturbed shear stress, and (2) helicity intensity (h_2) is protective against WT and has a potential in predicting atherosclerotic plaque growth. However, a gap in knowledge still exist on the significance of HF in human coronary arteries, a prominent site of atherosclerotic plaque formation. In this scenario, the aim of this study was to investigate if the relation between HF and disturbed shear, already emerged in in silico animal models, is confirmed in a representative sample of patient-specific computational models of coronary arteries. To do that, one non-stented non-culprit coronary artery (left anterior descending - LAD, left circumflex - LCX, or right coronary artery - RCA) of hemodynamically stable patients with an acute coronary syndrome was imaged by computed tomography angiography and intravascular ultrasound (IVUS). The geometry of the 49 imaged coronary arteries was reconstructed. The finite volume method was used to numerically solve Navier-Stokes equations, by prescribing personalized boundary conditions (BCs) derived from Doppler flow velocity measurements. If flow measurements were not good enough, a generalized flow rate waveform was imposed as inflow BC. Three canonical descriptors of 'disturbed hemodynamics' based on the wall shear stress (WSS), i.e. time-averaged WSS (TAWSS), oscillatory shear index (OSI), and relative residence time (RRT) were computed. Objective thresholds for 'disturbed flow' were defined as the upper (lower) 33th percentile of pooled data for OSI and RRT (TAWSS). The percentage of luminal area exposed to 'disturbed flow' was quantified and labeled as *TAWSS33*, *OSI66*, and *RRT66*, respectively. Intravascular hemodynamics was investigated by applying different helicity-based descriptors, quantifying HF amount and topology. Additionally, local normalized helicity (LNH) was used to visualize intravascular HF structures. Regression analysis was used to identify possible relations between each pair of WSS- and helicity-based descriptors and reported as Spearman correlation coefficients. Results from this work suggested that (1) two distinguishable counter-rotating HF structures naturally develop all along the length of the human coronary artery, although with different intensity, and (2) among the investigated helicity-based hemody-

namic descriptors, the cycle-averaged helicity is strongly inversely associated with the percentage of surface area exposed to unfavorable shear conditions. In particular, h_2 was negatively associated ($r = -0.84$, $p < 0.001$) with *TAWSS33* and *RRT66* (i.e. lower helicity intensity implies larger lumen area exposed to low WSS and high RRT). These findings confirm previous evidence in coronary animal models, revealing that counter-rotating HF patterns physiologically develop also in human coronary arteries, and may be used as in vivo surrogate marker of disturbed flow.

Chapter 1

INTRODUCTION

Helical flow (HF) consists of a helical-shaped arrangement of the streaming blood (as given by the combination of translational and rotational blood flow motions) and it is known to markedly characterize arterial hemodynamics [2]. The acknowledgment of a beneficial nature to HF in arteries is consistent with the fundamental role recognized for helicity in the organization of both laminar and turbulent flows by the fluid mechanics theory.

It is known that arteries adapt to long term variations forces by dilatating and remodelling to a larger diameter when the forces increase, whereas they decrease in magnitude the intimal layer becomes thinner and consequently the diameter gets smaller. This mechanism is fundamental to establish a physiological condition in the vessel. With these information become evident that the blood flow plays a fundamental role in maintaining the normal functioning of the circulatory system. In particular, the focus is mainly on the physical stresses due to disturbed flow, that they could cause inflammations, infections or chemical abnormalities in the bloodstream.

There are a plenty of studies that involved human arteries, as shown in Figure 1.1. It was demonstrated that a predominantly single right-handed helical flow exihbited in the upper aortic arch of the healthy subjects in late systole [14]. Other scientists observed that flow in the descending thoracic aorta was chirally asymmetric with systolic clockwise and diastolic counterclockwise components [4]. In addition, computational fluid dynamic studies indicated that the helical flow patterns in human coronary artery is induced by its three dimensional curvature [13] [26], an aspect that it will be investigated in the thesis.

The variety of helical flow investigated in the human body led to research a physiological significance of it. The main assertions are that helical

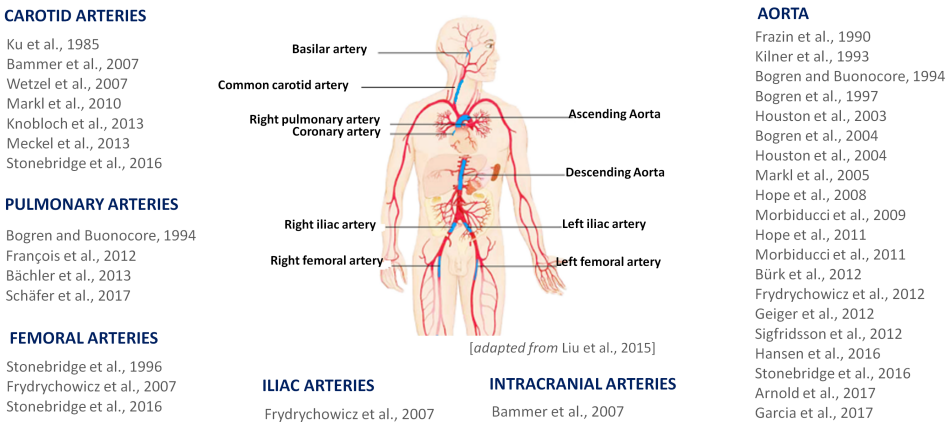

Figure 1.1: *Helical flow patterns already revealed based on in vivo studies.*

flow would facilitate blood flow transport, enhance mass transport in the arterial lumen and reduce accumulation and adhesion of blood cells on the arterial surface, which may protect from vascular diseases, in particular from atherosclerosis. Atherosclerotic lesions in the arterial wall mainly develop along the inner walls of curved segments or at the outer walls of arterial bifurcations, in particular where blood flow is disturbed and flow separation occur. The major elements that cause the lesions are the low density lipoproteins (LDLs), which is widely demonstrated as a cause also of stenoses of arterial lumen, thus leading to a disturbed flow and consequently to an accelerated platelet aggregation [16] [21]. In fact, in early stage of atherosclerosis a common phenomena is the accumulation of LDLs within the arterial walls so mass transport between wall and blood is a fundamental process. HF might uniform the WSS, thus inibiting flow stagnation and separation and thus leading to a better effectiveness of the mass transport. Compared to normal flow pattern, HF is more efficient and require less energy to drive blood through the arterial system [24], i.e. in aorta is demonstrated that it might reduce the energy dissipation, thus obtaining efficient perfusion and minimizing myocardial overloading [20]. Findings in carotid bifurcation and aorta confirmed that a high helical flow intensity suppresses flow disturbances, and thereby is potentially protective for atherosclerotic plaque build-up [3]. Hence, if not treated in time it will have a relevant impact on vascular disease i.e. ischaemic coronary artery disease (CAD), caused by destabilization and subsequent rupture of atherosclerotic plaques, is predicted to remain the leading cause of death. It is also notable that absence of HF in aorta is caused by carotid arterial diseases and eventually to short-term renal disfunction (renal arterial stenosis [10] [11]).

Besides human arteries experimentation, many researches was done on swine arteries, because their geometry is similar to the human's one. A lot of data comes from adult full-growth pigs (to exclude infuence of growth-related changes in the geometry of the coronaries, important for serial assessment of WSS), where the findings highlighted a significant association between the mean values of the WSS-based descriptors and helicity intensity, showing in detail, that high helicity intensity in the whole intravascular volume induces high mean TAWSS values along the luminal surface [9], and low wall thickness and wall thichness growth rate over time [2]. Another study inspected the relationship between wall thickness and helicity-based descriptors, highlighting that the growth of lipid-rich plaques (LDLs accumulation sites) is more frequent with low and oscillatory WSS, while the growth of the fibrotic plaques are independent of WSS [9]. These information can be summarized by stating that plaque initiation and plaque progression are associated with low TAWSS and high levels of multidirectionality, both in midly and advanced disease status [9].

In this study was evaluated the quantitative amount of helical blood flow, and it was investigated which correlations exist among helical flow, vascular geometry and descriptors of disturbed shear stress in a representative sample of human-specific computational hemodynamic models of coronary arteries. The aim is to evaluate which relationship exist between them in the human coronary arteries, branch of the arterial system still little indagated.

Chapter 2

MATERIALS AND METHODS

2.1 *Population and Imaging*

Fourty-nine hemodynamically stable patients with acute coronary sindrome (ACS) with at least one non-stented non-culprit coronary segment accessible for intracoronary imaging were enrolled in the study. Exclusion criteria included the presence of previous coronary artery bypass graft surgery, 3-vessel disease, renal insufficiency, left ventricular ejection fraction $< 30\%$, and atrial fibrillation. All patients were treated with percutaneous coronary intervention (PCI) of the culprit lesions. After successful treatment, a non-culprit segment per patient was imaged by intravascular ultrasound (IVUS) and coronary computed tomography angiography (CTA). Furthermore, ComboWire Doppler flow measurements were performed along each coronary vessel. An overview of the methods is provided in Figure 2.1. The study protocol was approved by the local medical ethical committee of the Erasmus MC (MEC 2015-535, NL54519.078.15), and the study was conducted in accordance with the World Medical Association Declaration of Helsinki (64th WMA General Assembly, Fortaleza, Brazil, October 2013) and Medical Research Involving Human Subject Act (WMO) [7].

2.2 *Geometry Reconstruction*

Forty-nine patient-specific coronary artery models were reconstructed for the analysis (one per patient). Both CTA and IVUS images were used to reconstruct 18 left descending (LAD), 13 left circumflex (LCX), and 18 right

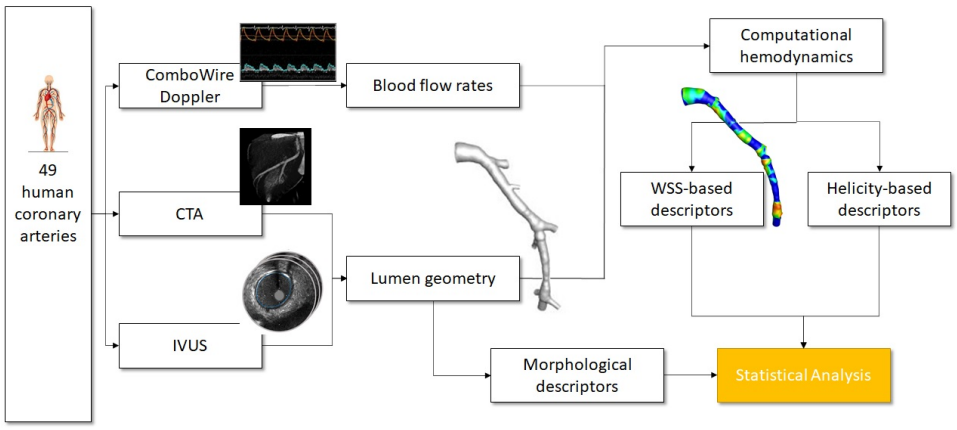

Figure 2.1: *Schematic diagram of the thesis design. CTA: computer tomography angiography; IVUS: intravascular ultrasound.*

(RCA) coronary arteries. In detail, vessel lumen contours were segmented on the IVUS images using QCU-CMS software, and then positioned orthogonal to the 3D centerline extracted from CTA images using Mevislab software. As sketched in Figure 2.2 [3], IVUS and CTA images were matched basing on the side branches as biological landmarks [23]. An off-line ECG gating was performed using an in-house algorithm implemented in Matlab environment, since IVUS pullbacks were not in vivo gated. The latter avoided reconstruction artefacts caused by the heartbeat. One IVUS frame was selected per cardiac cycle, in the same diastolic phase. In addition, CTA images were segmented to reconstruct luminal region proximal (up to the aorta) and distal (at least two diameters) to the IVUS-imaged segment. A semi-automatic segmentation method was applied [23]. All visible side branches were reconstructed. Finally, to improve the quality of the 3D reconstruction, in some cases local smoothing was applied at the IVUS-CTA transitions and at the attachment regions of the side branches. Further details are reported elsewhere [3] [2] [9] [7]. The resulting geometries are displayed in Figure 2.3.

2.3 *Computational Hemodynamic*

2.3.1 *Computational Meshes*

The meshes were obtained by means of 6.5 millions (on average) tetrahedrons with a curvature-based refinement and a 5-layer prism at the lumen, using the computational fluid dynamics code Fluent (ANSYS INc., Canonsburg,

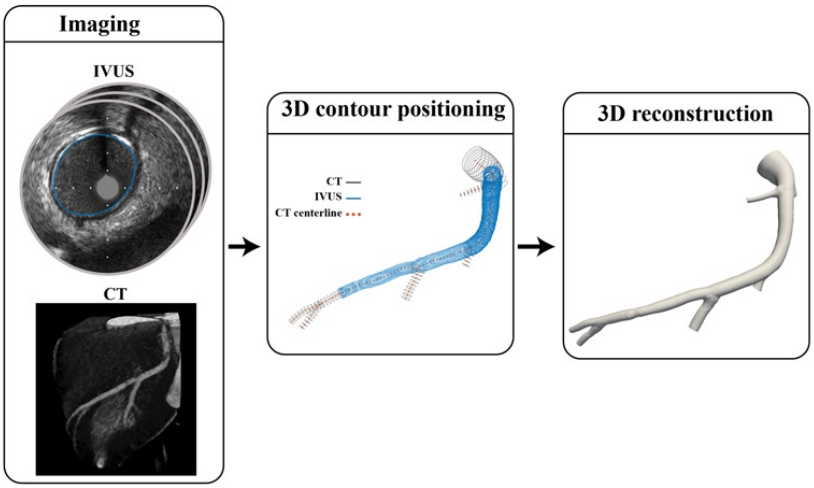

Figure 2.2: *Scheme applied for the coronary artery geometry reconstruction from CT and IVUS images.*

PA, USA) [3]. An example of the applied mesh strategy of the vessel and inner region is presented in Figure 2.4, Figure 2.5 [3]. Meshing procedure is extensively detailed in previous works [3] [2] [9].

2.3.2 *Finite Volume Method*

The finite volume method was used to numerically solve Navier-Stokes equations (Eq 2.1) by prescribing personalized boundary conditions.

$$\begin{cases} \nabla \cdot u = 0 \\ \rho \left[\dfrac{\partial u}{\partial t} + u \left(\nabla \cdot u \right) \right] = -\nabla p - \left[\nabla \cdot \bar{\bar{\tau}} \right] \end{cases} \tag{2.1}$$

where u is the velocity vector $[m/s]$, μ is viscosity $[kg/(m\ s)]$, ρ is density $[kg/m^3]$, p is pressure $[Pa]$, τ is the stress tensor.

The boundary conditions imposed derived from *in vivo* Doppler velocity measurements. The flow rate was measured at several locations upstream and downstream of each side branch with ComboWire. As condition of the inflow BC was choosen the most proximal measurement-based flow rate in terms of time-dependent flat velocity profile [3]. The measurement was done

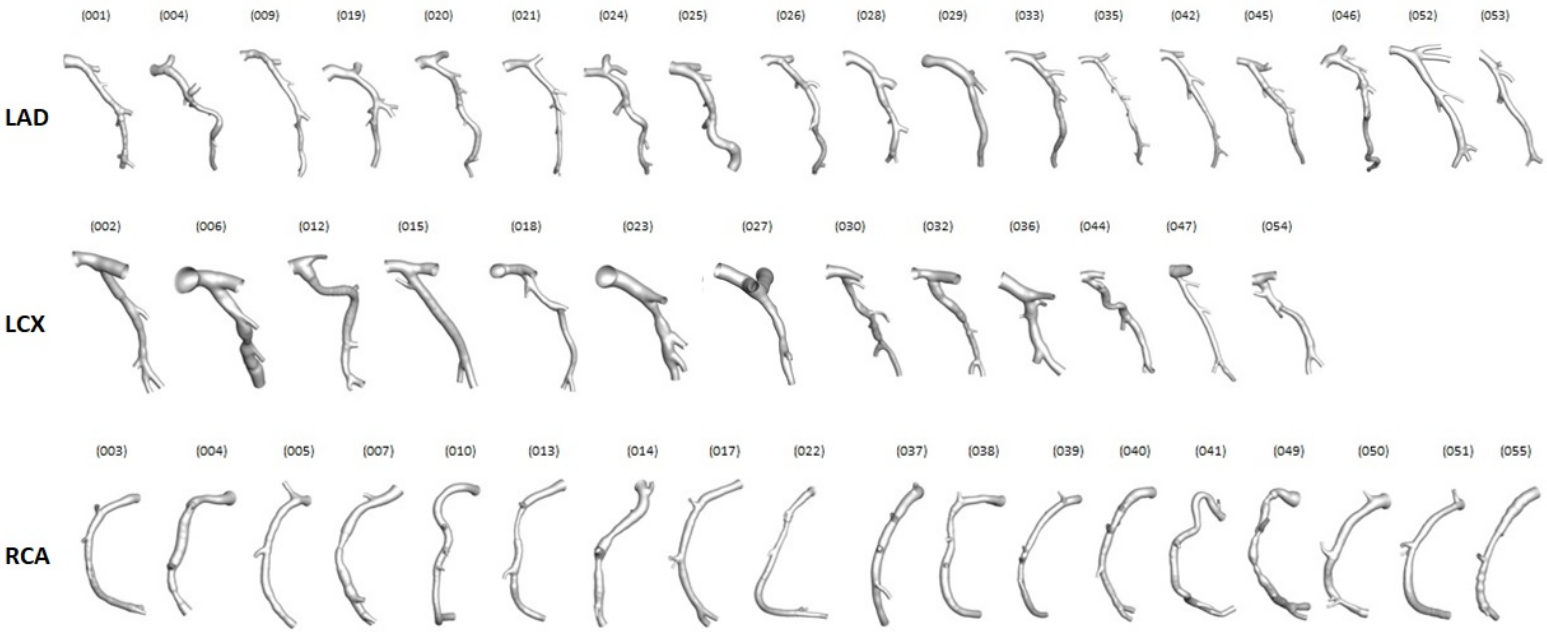

Figure 2.3: *Geometry of the fourty-nine human coronary arteriy models.*

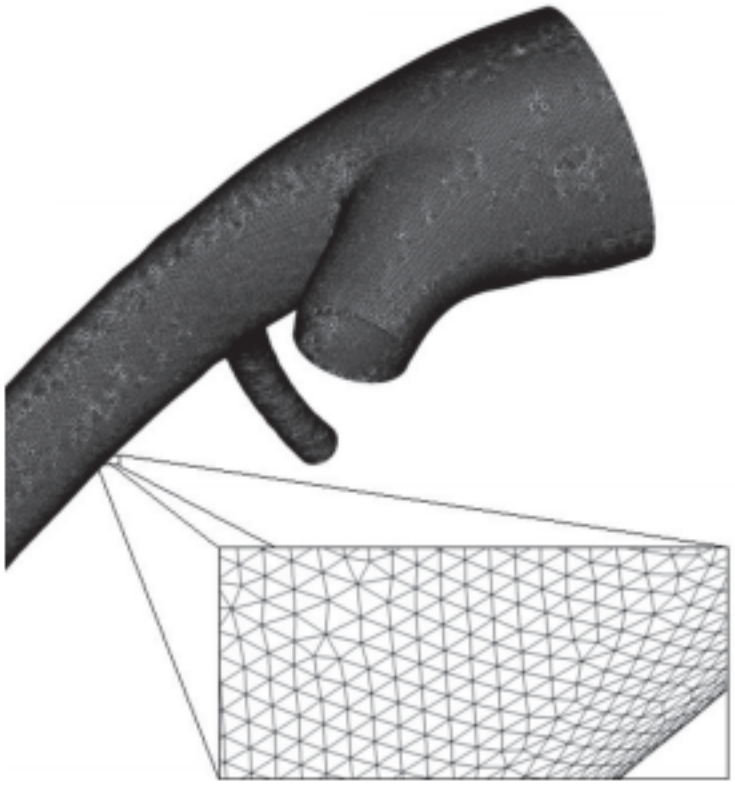

Figure 2.4: *Design of the mesh in the vessel region.*

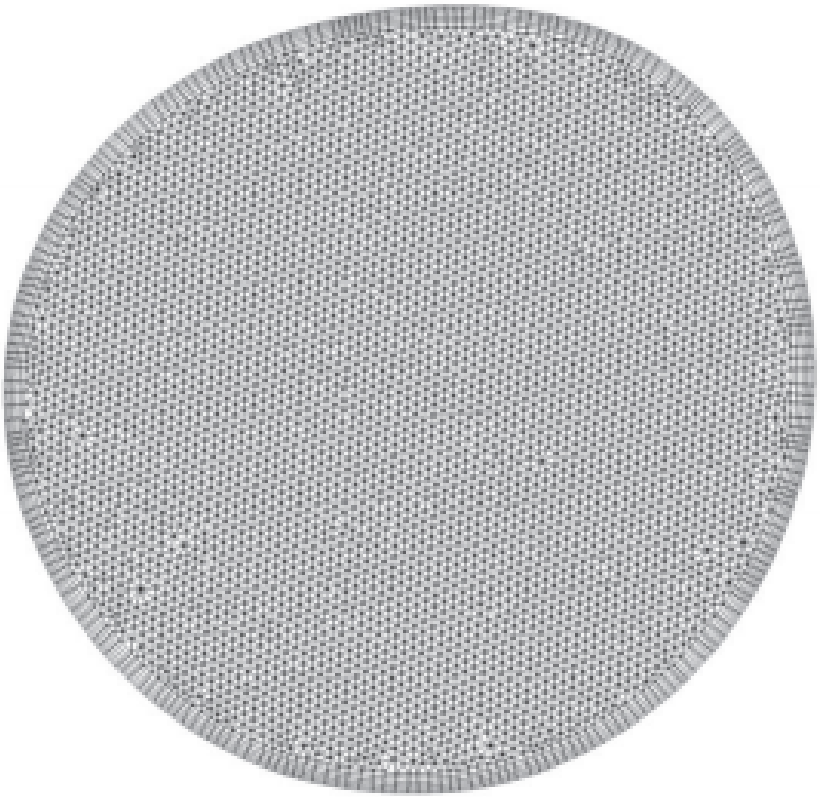

Figure 2.5: *Design of the mesh in the inner region.*

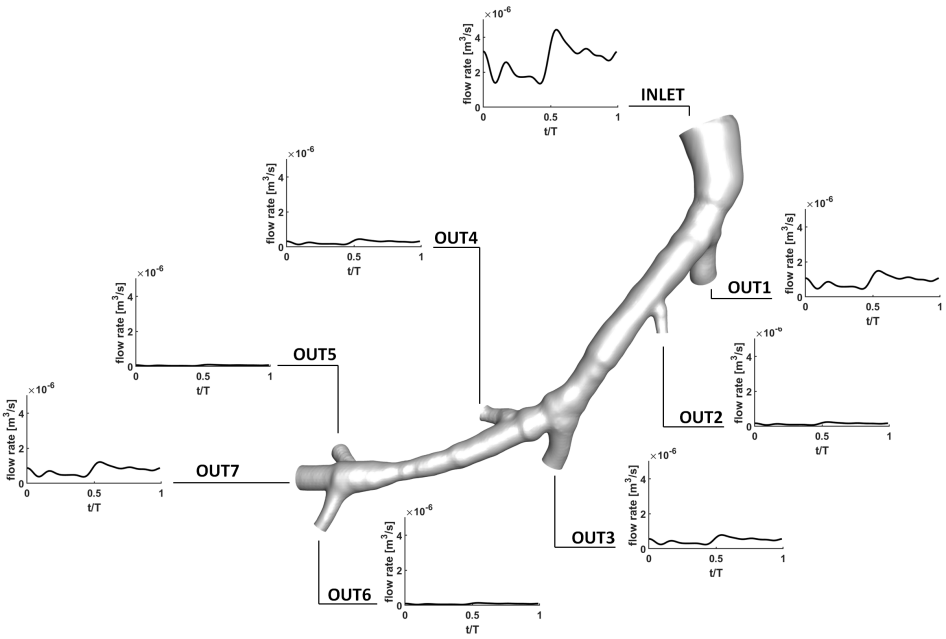

Figure 2.6: *Details of the applied boundary conditions for case 001LAD.*

also for each side branch and if it was accurate enough it was imposed as outlet BC, on the contrary, using a described scaling law -the Huo-Kassad diameter-based scaling law [12]- was estimated the flow ratio between the mother and the side branch and that was prescribed.
An example of a specific (case 001LAD) applied boundary condition is shown in Figure 2.6.

Blood was assumed as an incompressible, homogeneous fluid with density ρ equal to 1060 kg/m^3 and its non-Newtonian behavior was modeled assuming it as a Carreau fluid [3]. The Carreau model is employed for representing the shear-thinning property of blood viscosity. The relationship between viscosity and shear rate is given by:

$$\mu(\dot{\gamma}) = \mu_\infty + (\mu_0 - \mu_\infty)[1 + (\lambda\dot{\gamma})^2]^{(n-1)/2} \tag{2.2}$$

where μ_∞=0.0035 $[kg/(m\ s)]$ and μ_0=0.25 $[kg/(m\ s)]$ are the infinite and zero shear rate limit viscosities respectively, λ=25 $[s]$ is the relaxation time constant and n=0.25 is the power law index.
At the arterial wall was assumed that the fluid completly stops (no-slip condition).

2.4 *Post-Processing*

The 49 models were post-processed in the main branch only. To do that, it was used the open-source Vascular Modeling Toolkit (VMTK). In particular, it was identified the centerline [**Def.** *locus of centers of cross-sections of the pipe entrance effect due to a change in the vessel*] for each branch, for each model, and side branches were removed by cutting their centerlines. This procedure was used for both surfaces (for the calculation of the WSS-based descriptors) and meshes (for the calculation of the helicity-based descriptors).

2.4.1 *WSS-Based Descriptors*

The Wall Shear Stress (WSS), τ_w, given by Eq 2.3, is the most important hemodynamics force because the adaptation process to long term of arteries mostly depends on it.

$$\tau_w = \mu \left(\frac{\partial u}{\partial y} \right)_{y=0} \tag{2.3}$$

where μ is the dynamic viscosity, u is the velocity parallel to the wall and y is the distance to the wall.
WSS plays an important role in the development and progression of vessel wall pathologies, in fact it has been demonstrated that low mean shear stress and marked oscillations in the direction of WSS could be critical factors in the localization and development of atherosclerosis plaques. Furthermore, WSS has effects on endothelial cells. According to the level of WSS there is a changing in the alignment of the endothelial cells: where the flow is laminar, the cells elongate and align in the direction of the flow, while in the case of low and oscillatory WSS they assume a disordered and polygonal orientation.
Therefore, in recent years hemodynamics indicators were introduced to enable a quantitative analysis of blood flow patterns in arteries [18], in particular, to describe the multidirectional flow behaviour.
The first and most relevant descriptor is the Time-Averaged Wall Shear Stress (**TAWSS**). It is calculated by integrating each nodal WSS vector magnitude at the luminal surface over the cardiac cycle (see Table 2.1). For this parameter, three ranges of interest can be distinguished: low values,

moderate values and high values. The first delineate a pro-atherogenic endothelial phenotype, the second induce an atheroprotective gene expression profile, the third can cause endothelial trauma.
The second descriptor is the Oscillatory Shear Index (**OSI**). It is a useful parameter for the identification of regions on the vessel wall that are subject to highly oscillating WSS values during the cardiac cycle. High values (with a maximum of 0.5 (see Table 2.1)) highlight regions where the WSS deviates istantly from the main flow direction, for instance in proximity of bifurcations or areas with vortex formation.
The last most important parameter is the Relative Residence Time (**RRT**). Its formula is defined in Table 2.1 and it shows that it is inversely proportional to the magnitude of the time-averaged WSS vector.
Finally, the luminal distribution of three "established" WSS-based descriptors, (**TAWSS**), (**OSI**) [15], and (**RRT**) [8] was computed.

Table 2.1: *Definition of WSS-based hemodynamic descriptors.*

Time Averange WSS (TAWSS)	$\mathrm{TAWSS} = \frac{1}{T}\int_0^T \lvert\mathbf{WSS}\rvert \, dt$
Oscillatory Shear Index (OSI)	$\mathrm{OSI} = 0.5\left[1 - \left(\frac{\left\lvert\int_0^T \mathbf{WSS}\, dt\right\rvert}{\int_0^T \lvert\mathbf{WSS}\rvert \, dt}\right)\right]$
Relative Residence Time (RRT)	$\mathrm{RRT} = \frac{1}{\mathrm{TAWSS}\cdot(1-2\cdot\mathrm{OSI})} = \frac{1}{\frac{1}{T}\left\lvert\int_0^T \mathbf{WSS}\, dt\right\rvert}$

WSS is the WSS vector; T is the period of the cardiac cycle.

2.4.2 *Helicity-Based Descriptors*

Helical flow in the 49 coronary artery models was characterized by applying different helicity-based descriptors, listed in Table 2.2.
Average helicity descriptors h_1 and h_2 indicate the net amount and the intensity of helical flow, respectively. The first is an integral measure of helical flow accounting for changes in sign of $\mathrm{H_k}$. Therefore, h_1 equals 0 in the presence of reflectional symmetry in the fluid domain [6]. The helicity intensity h_2 is an indicator of the total amount of helical flow in the fluid domain, irrespective of direction [6]. The helical rotation balance descriptors measure

the prevalence (identified by the sign of descriptor h_3) or only the strength (h_4) of relative rotations of helical flow structures. Descriptor h_3 measures the prevalence of the helical rotation, it is a non-dimensional quantity ranging between (-1) and 1: its value equals (-1) (+1) when only left-handed (right-handed) helical structures are present in the domain and it equals 0 in case of reflectional symmetry [6]. Descriptor h_4 ignores the major direction of rotation, it is calculated as the absolute value of h_3, varying between 0 and 1. Finally, h_5 is defined as the ratio between the volume of the fluid in the dominant direction ($\mathrm{V_{id}}$) of rotation and the volume occupied by helical patterns rotating in the minor direction of rotation ($\mathrm{V_{im}}$), while h_6 is the ratio between the mean volumetric helicity values over the volume occupied by the dominant and the minor direction of rotation.

Table 2.2: *Definition of helicity-based intravascular hemodynamic descriptors.*

Average helicity (h_1)	$\frac{1}{V}\int_{T_i}\int_{V_i} H_k \, dV \, dt$
Average helicity intensity (h_2)	$\frac{1}{V}\int_{T_i}\int_{V_i} \lvert H_k \rvert \, dV \, dt$
Signed balance of counter-rotating helical flow structures (h_3)	$\frac{h_1}{h_2}$
Unsigned balance of counter-rotating helical flow structures (h_4)	$\lvert h_3 \rvert = \frac{\lvert h_1 \rvert}{h_2}$
Volume of the fluid domain ratio (h_5)	$\frac{\int_{T_i}\int_{V_{id}} dV_d \, dt}{\int_{T_i}\int_{V_{im}} dV_m \, dt}$
Mean volumetric helicity ratio (h_6)	$\frac{\frac{1}{V_d}\int_{T_i}\int_{V_{id}} H_{kd} \, dV_d \, dt}{\frac{1}{V_m}\int_{T_i}\int_{V_{im}} H_{km} \, dV_m \, dt}$

H_k is the helicity vector ($= \mathrm{v} \cdot \omega$); where v and ω are defined in the adapted Figure 2.7 [2].

The quantitative analysis, based on the hemodynamic descriptors mentioned above, was substantiated by visualizations of near-wall and intravas-

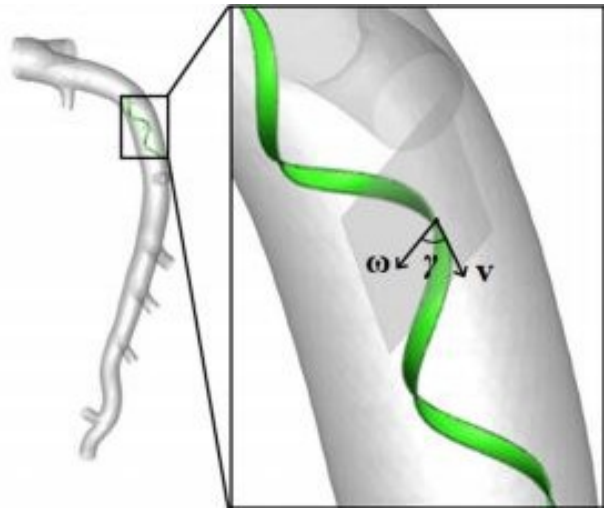

Figure 2.7: *v is the velocity vector, ω is the vorticity vector. The angle γ indicates the circumferential direction around the arterial lumen. The top of the graph is the proximal region, while the bottom one is the distal region of the artery.*

cular quantities. The normalized internal product between local velocity and vorticity vectors (see the adapted Figure 2.7 [2]), labeled as local normalized helicity (**LNH**) [19],

$$\mathrm{LNH} = \frac{\mathrm{v} \cdot \omega}{|\mathrm{v}| \cdot |\omega|} = \cos\gamma \tag{2.4}$$

was used to visualize helical blood flow inside the coronary segments. The LNH allows to visualize left- and right-handed fluid structures in arteries and isosurfaces of cycle average LNH values that were used in the thesis.

2.4.3 *Morphometric Descriptors*

The centerlines of the clipped models were extracted using VMTK. To obtain a free noise analytical formulation of curve $\boldsymbol{C}$ with continuous derivates that was compared with the vessel centerlines extracted, it was used a free-knots regression splines [22]. At this point, two parameters are the most representative for the morphometric description. Local curvature κ is defined as the reciprocal of the radius of the circle lying on the osculating plane. Local torsion τ measures the deviation of curve $\boldsymbol{C}$ from the osculating plane. Both the quantities are calculated along the curvilinear abscissa s with the following formulas:

$$\kappa(s) = \frac{|C'(s) \times C''(s)|}{|C'(s)|^3} \tag{2.5}$$

$$\tau(s) = \frac{|C'(s) \times C''(s)| \cdot C'''(s)}{|C'(s) \times C''(s)|^2} \tag{2.6}$$

where ***C'(s)***, ***C"(s)*** and ***C"'(s)*** are the first, second and third derivative of curve ***C***, respectively. After that the average values are calculated because, as we know from previous knowledge, they are representative of the trend in the vessel [1].

2.5 *Statistical Description*

All the following operations were performed in Matlab environment (The MathWorks Inc., USA).

A statistical representation of each WSS descriptor was initially done to have an idea of the possible values and scale variations.

Then, the probability density function was calculated for each model and for each descriptor. These functions were used to identify the previously mentioned objective thresholds: the most representitive percentile. For TAWSS was the 33th percentile, named *TAWSS33*, that represents the value below that is the 33% of TAWSS distribution. For OSI and RRT was the 66th percentile, named as *OSI66* and *RRT66* respectively, that represent the value above that is the 66% of the distribution.

Finally, bivariate correlations among WSS-based, helicity-based and geometric descriptors were determined by using Spearman rank ordering. The same correlation method was used to identify the relationship between each pair for descriptors. Significance was assumed for $p < 0.05$.

Chapter 3

RESULTS

3.1 *WSS-based descriptors*

In the first part of the intra-individual analysis WSS-based descriptors were computed on the clipped models. In Figure 3.1 are shown the TAWSS distributions of the entire dataset, while in Figure 3.2 and Figure 3.3 are shown for OSI and RRT, respectively.

The first statistical analysis was aimed to evaluate mean values and respective standard deviation for each model. In Figure 3.4 are shown the results for TAWSS, in Figure 3.5 for OSI, in Figure 3.6 for RRT. Unfortunately, the results did not reveal a clear distinction in terms of model type. For this reason the next step was the evaluation of objective thresholds. For the choice there were calculated the pdf for each descriptor and a certain percentile that was descriptive was evaluated. For TAWSS the choosen one was the 33th percentile, for OSI was the 66th percentile and for RRT was the 66th percentile too. The pdf was initially calculated for all the 49 models separately (from Figure 3.7 to Figure 3.15) and finally for the pooled data (from Figure 3.16 to Figure 3.18). These values were finally chosen as thresholds and they are respectively 0.5854 Pa defined as *TAWSS33*, 0.0012 defined as *OSI66* and 1.6845 Pa^{-1} defined as *RRT66*.

In Figure 3.19 are visualized the surface areas (SA) exposed to low TAWSS ($<$ *TAWSS33*), while in Figure 3.20 the SAs exposed to high OSI ($>$ *OSI66*) and finally, in Figure 3.21 the SAs exposed to high RRT ($>$ *RRT66*). Red color highlights those areas exposed to low TAWSS, and high OSI, RRT. Percentages for all models are shown from Figure 3.22 to Figure 3.24. The following statements are evaluable from all these informations.

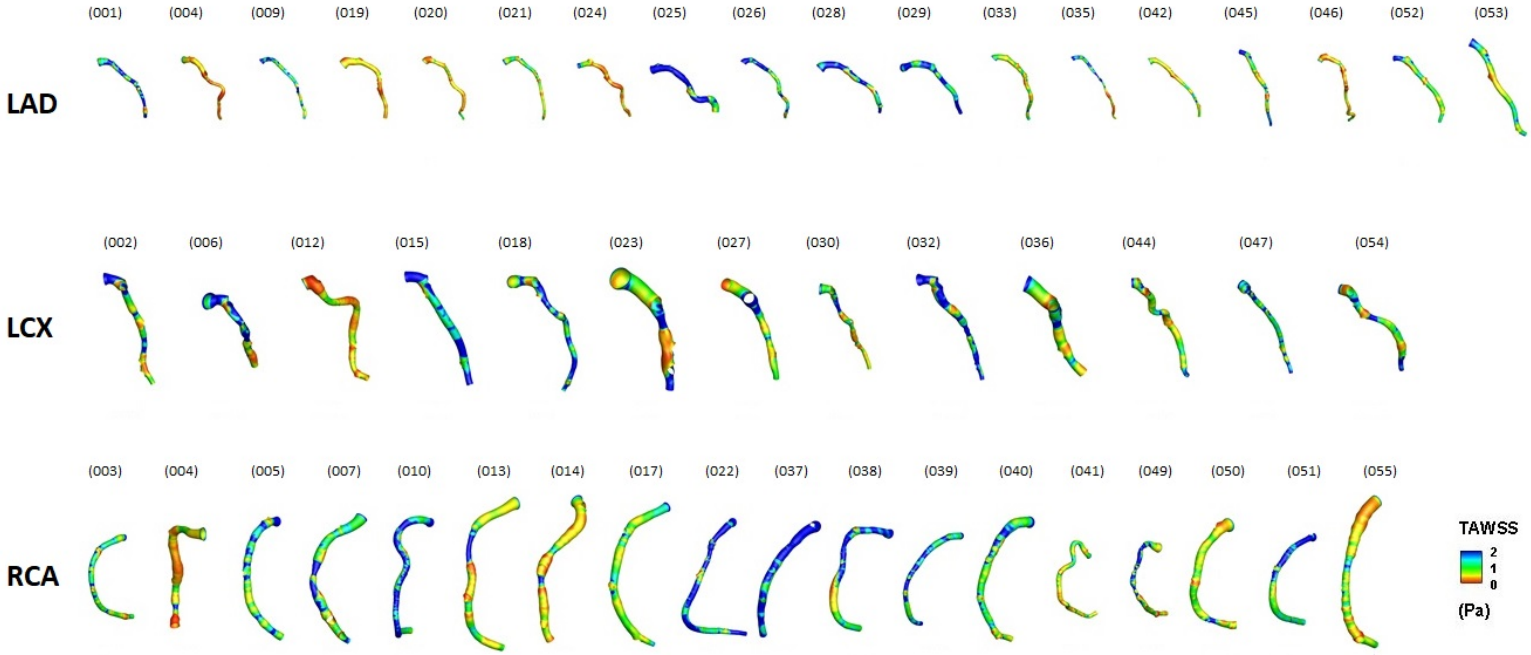

Figure 3.1: *TAWSS descriptor distribution at the luminal surface of all the 49 models divided into the three different types of coronary arteries.*

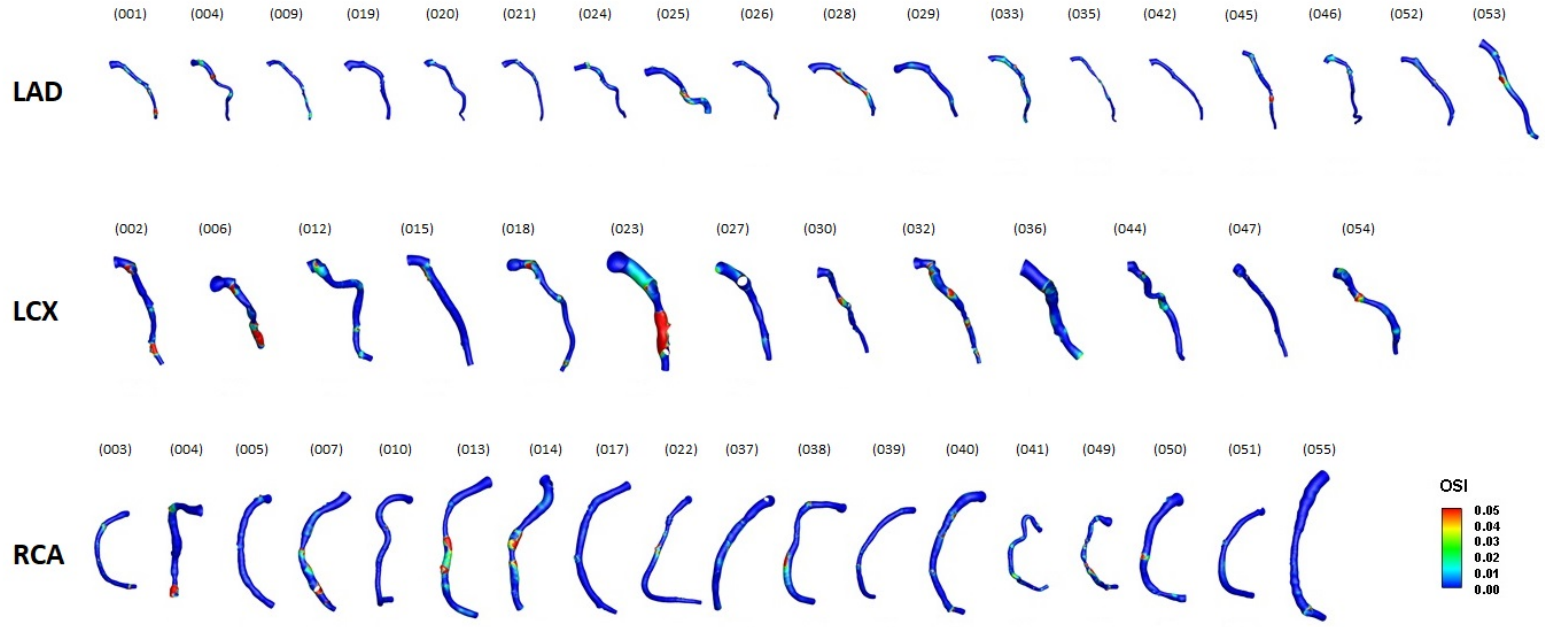

Figure 3.2: *OSI descriptor distribution at the luminal surface of all the 49 models divided into the three different types of coronary arteries.*

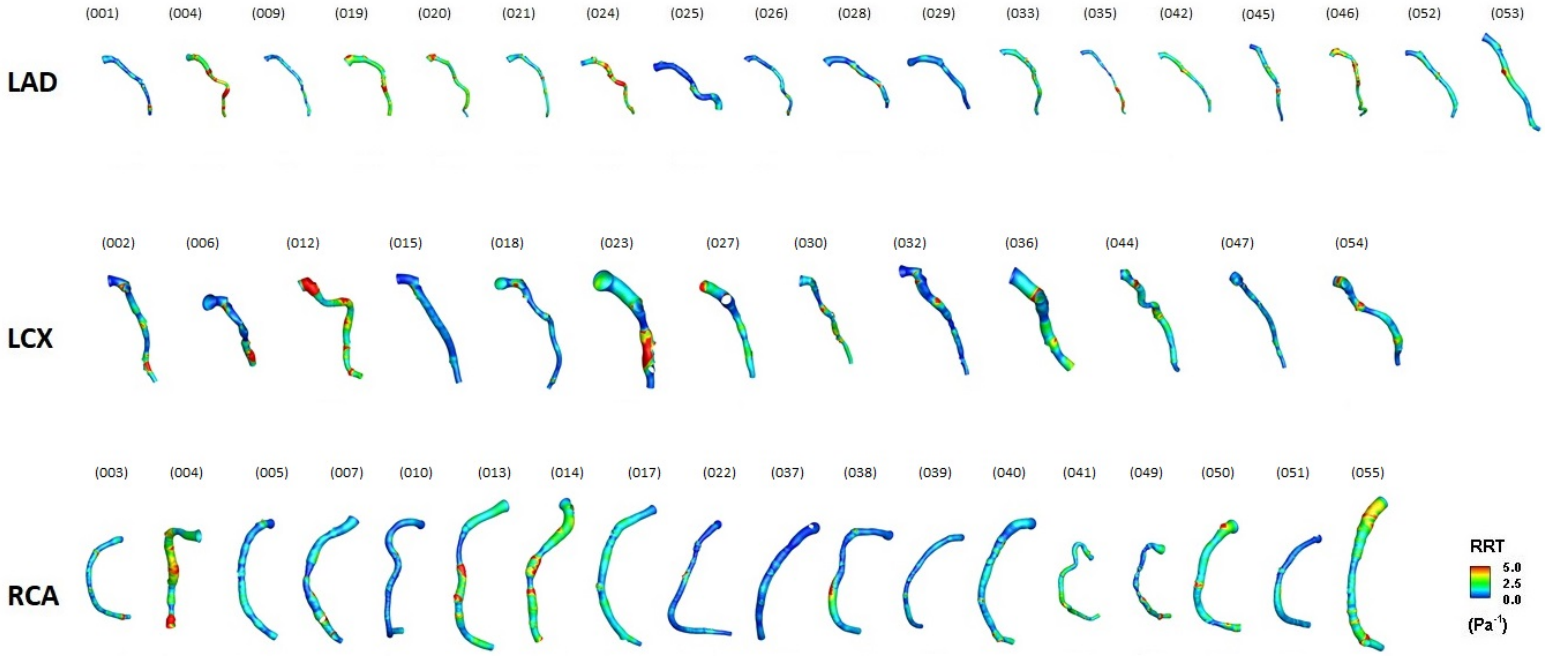

Figure 3.3: *RRT descriptor distribution at the luminal surface of all the 49 models divided into the three different types of coronary arteries.*

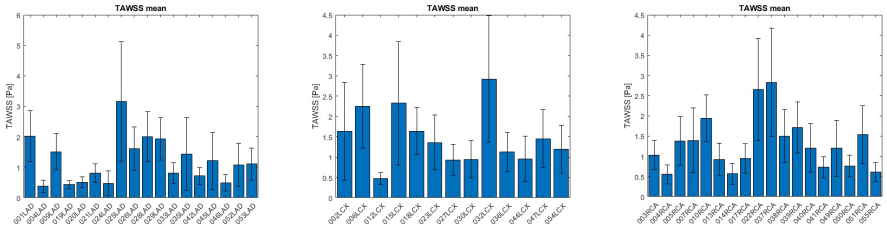

Figure 3.4: *Statistical representation of the TAWSS mean value and their standard deviation for each model.*

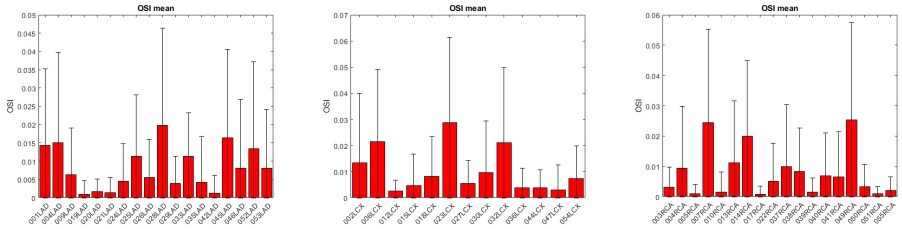

Figure 3.5: *Statistical representation of the OSI mean value and their standard deviation for each model.*

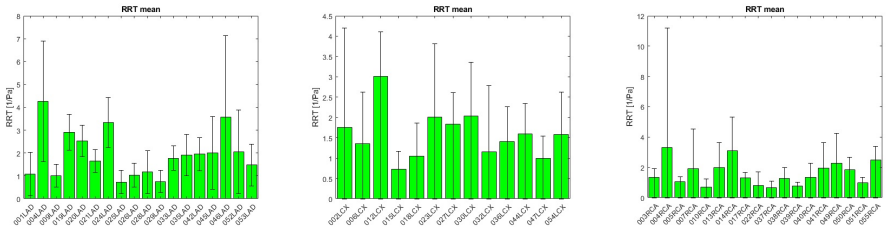

Figure 3.6: *Statistical representation of the RRT mean value and their standard deviation for each model.*

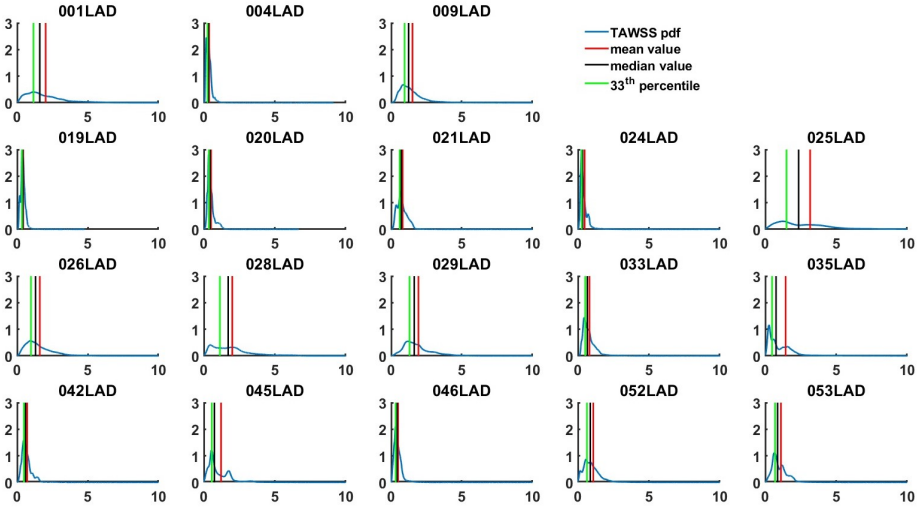

Figure 3.7: *Probability Density Functions of the TAWSS descriptor in each one of LAD coronary arteries.*

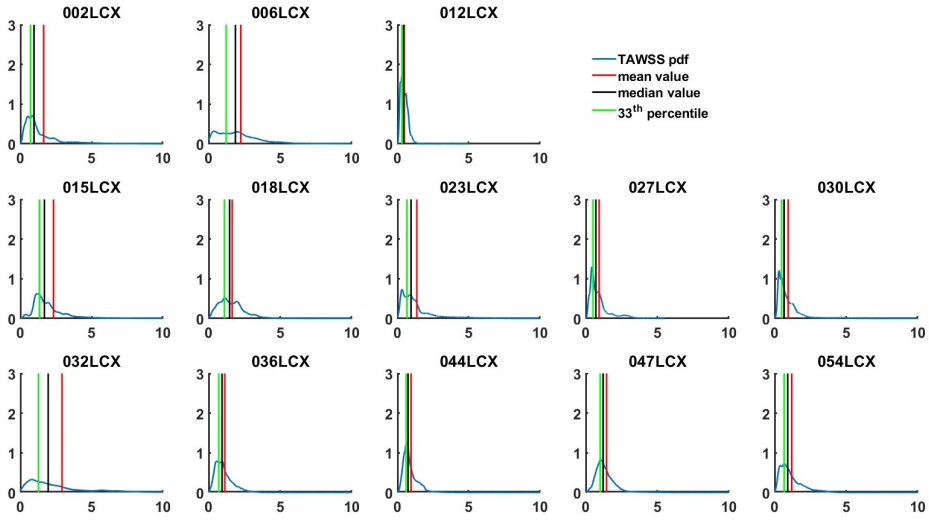

Figure 3.8: *Probability Density Functions of the TAWSS descriptor in each one of LCX coronary arteries.*

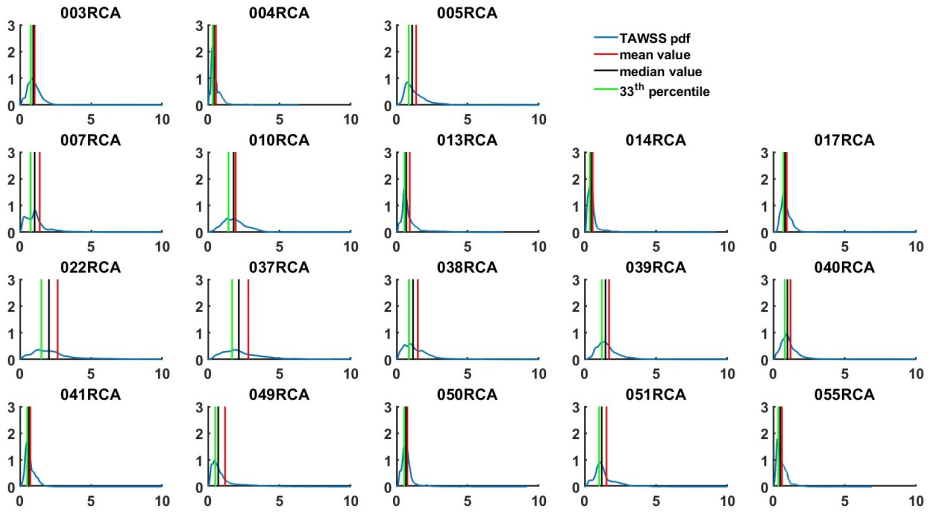

Figure 3.9: *Probability Density Functions of the TAWSS descriptor in each one of RCA coronary arteries.*

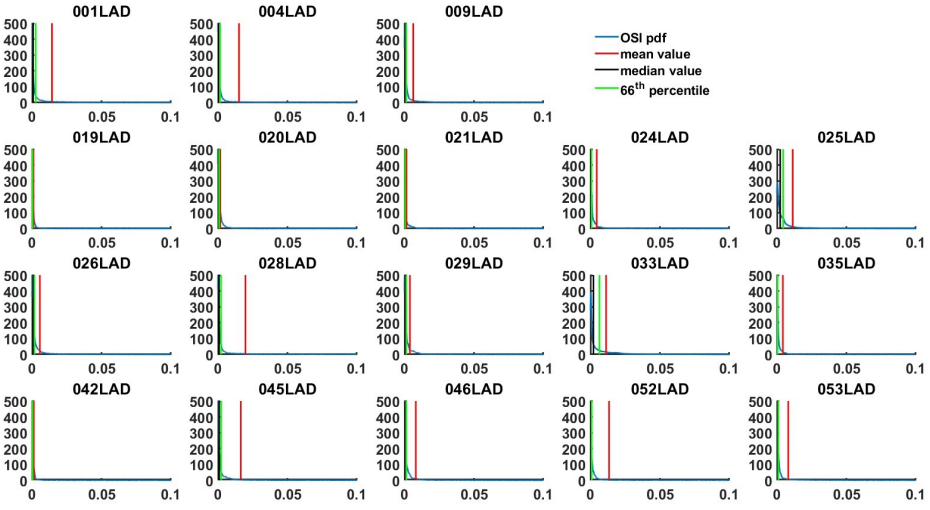

Figure 3.10: *Probability Density Functions of the OSI descriptor in each one of LAD coronary arteries.*

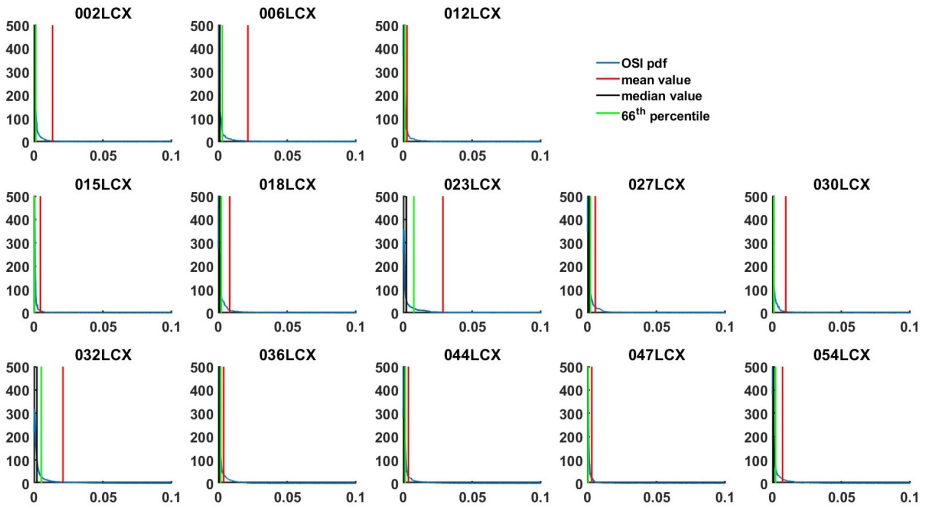

Figure 3.11: *Probability Density Functions of the OSI descriptor in each one of LCX coronary arteries.*

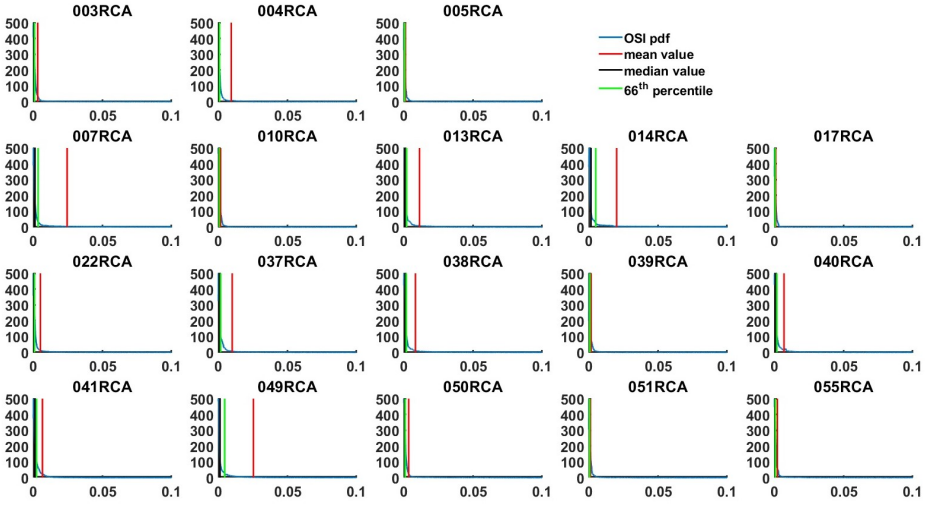

Figure 3.12: *Probability Density Functions of the OSI descriptor in each one of RCA coronary arteries.*

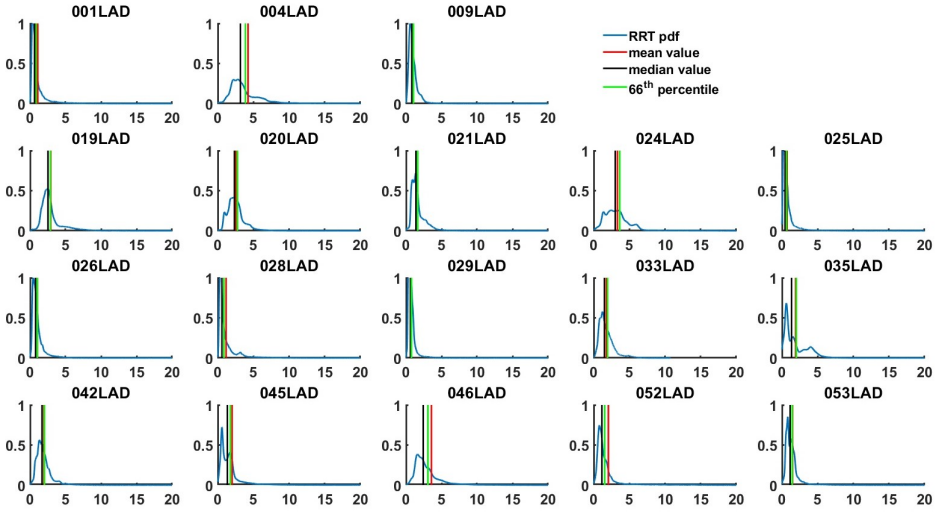

Figure 3.13: *Probability Density Functions of the RRT descriptor in each one of LAD coronary arteries.*

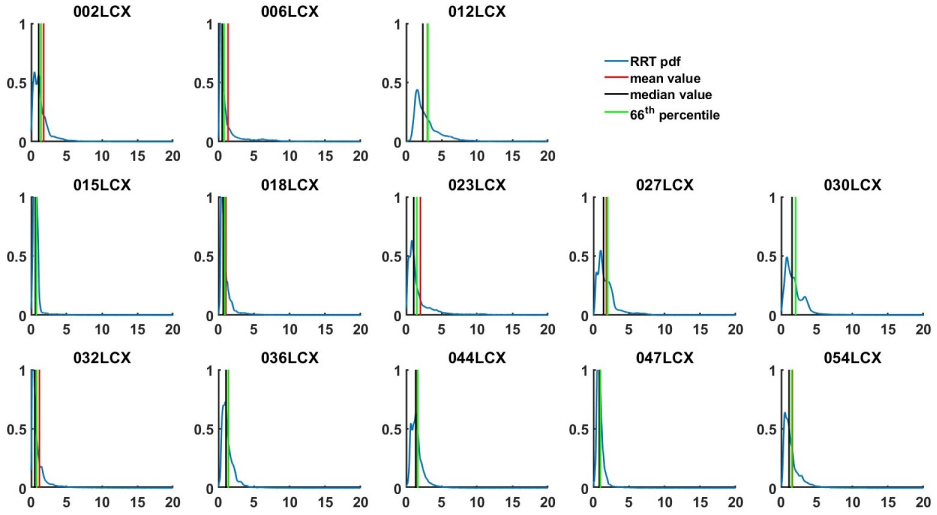

Figure 3.14: *Probability Density Functions of the RRT descriptor in each one of LCX coronary arteries.*

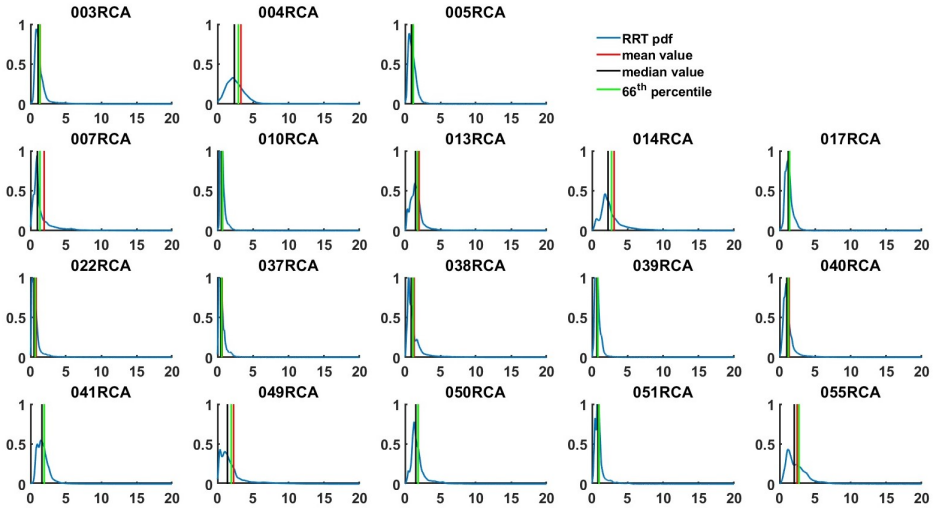

Figure 3.15: *Probability Density Functions of the RRT descriptor in each one of RCA coronary arteries.*

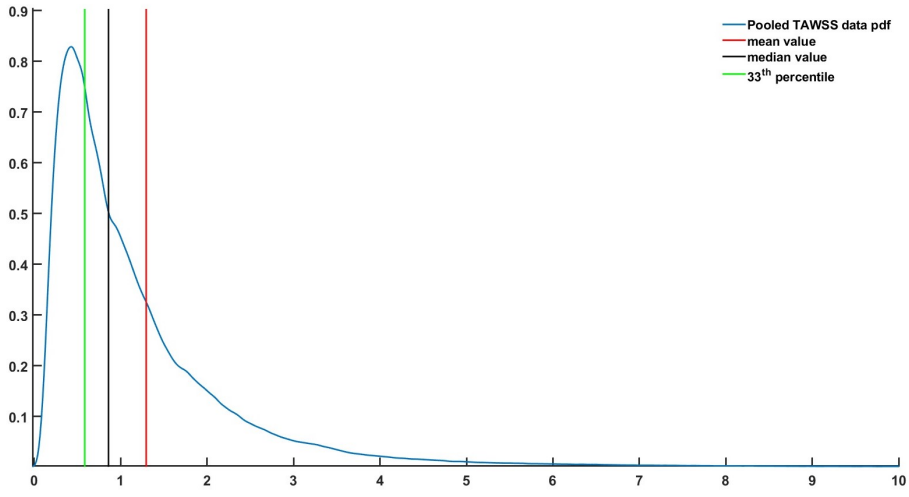

Figure 3.16: *Probability Density Functions of the pooled TAWSS data.*

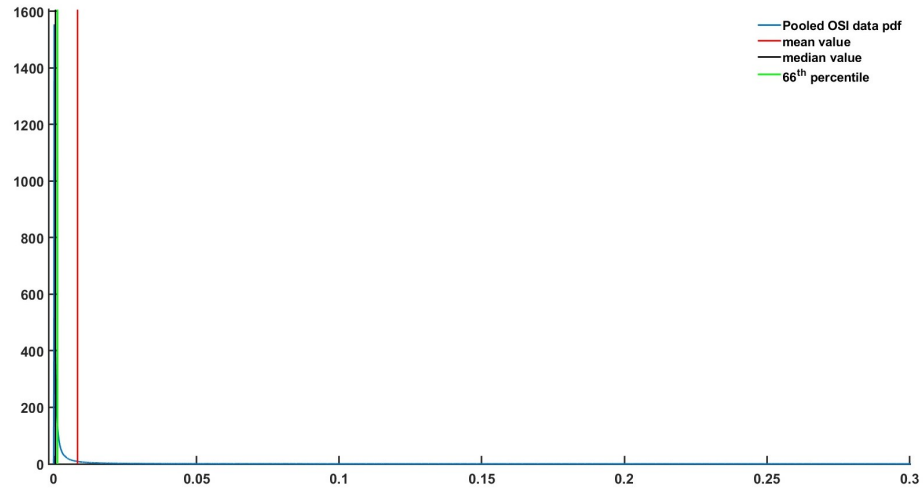

Figure 3.17: *Probability Density Functions of the pooled OSI data.*

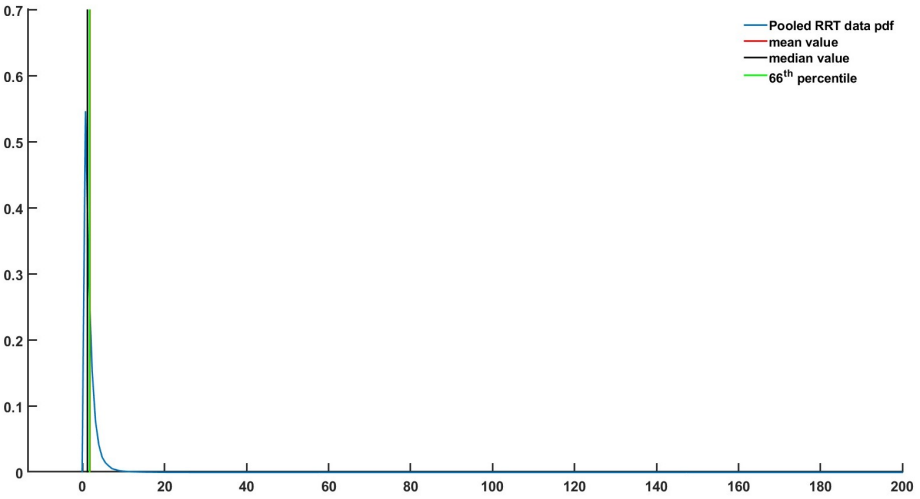

Figure 3.18: *Probability Density Functions of the pooled RRT data.*

TAWSS and RRT have a similar distribution, independent of coronary artery type, as expected in other studies. [3] While, as concern about OSI is evident that almost all models present low values. These results suggest that WSS is scarsely multidirectional in all the three different types of coronary arteries, thus suggesting a predominant role of low WSS as hemodynamic determinant of plaque formation in coronary arteries.

3.2 *Helicity-based descriptors*

Helical blood flow patterns were visualized using the isosurface of cycle-average LNH, with blue and red colors indicating left-handed and right-handed helical flow rotation, respectively [3]. In Figure 3.25 are shown all the 18 LADs, 13 LCXs and 18 RCAs models.
It is notable that exsist two distinguishable counter-rotating helical flow structures in each coronary artery. These structures are mostly distributed all along the length of the artery, except for a few models where LNH seems absent in the linear stretches. In some cases is also notable that in proximity of the bifurcation there is a turning in the rotation's direction.

Table 3.1: *Correlation coefficients between each couple of disturbed shear stress parameters (% surface area exposed) and geometry (average curvature and torsion) descriptors.*

	%OSI66	%RRT66	$\bar{\kappa}$	$\bar{\tau}$
%TAWSS33	0.20	**1.00**‡	**0.32***	-0.12
	%OSI66	0.21	0.18	-0.08
		%RRT66	0.32	-0.12
			$\bar{\kappa}$	-0.07

Statistically significant values are in bold.
$^{*}p < 0.05$; $^{\dagger}p < 0.01$; $^{\ddagger}p < 0.001$.

Bivariante correlation by using Spearman rank ordering was computed firstly for each couple of disturbed shear stress (Table 3.1). The only strong association that emerged is between *%TAWSS33* and *%RRT66*, notable to the fact that since OSI is low and non oscillatory in the investigated arteries, RRT is defined as inversely proportional to TAWSS. This results is confirmed also by comparing Figure 3.22 and Figure 3.24, where is evident that the differ only in the presence of a bias.

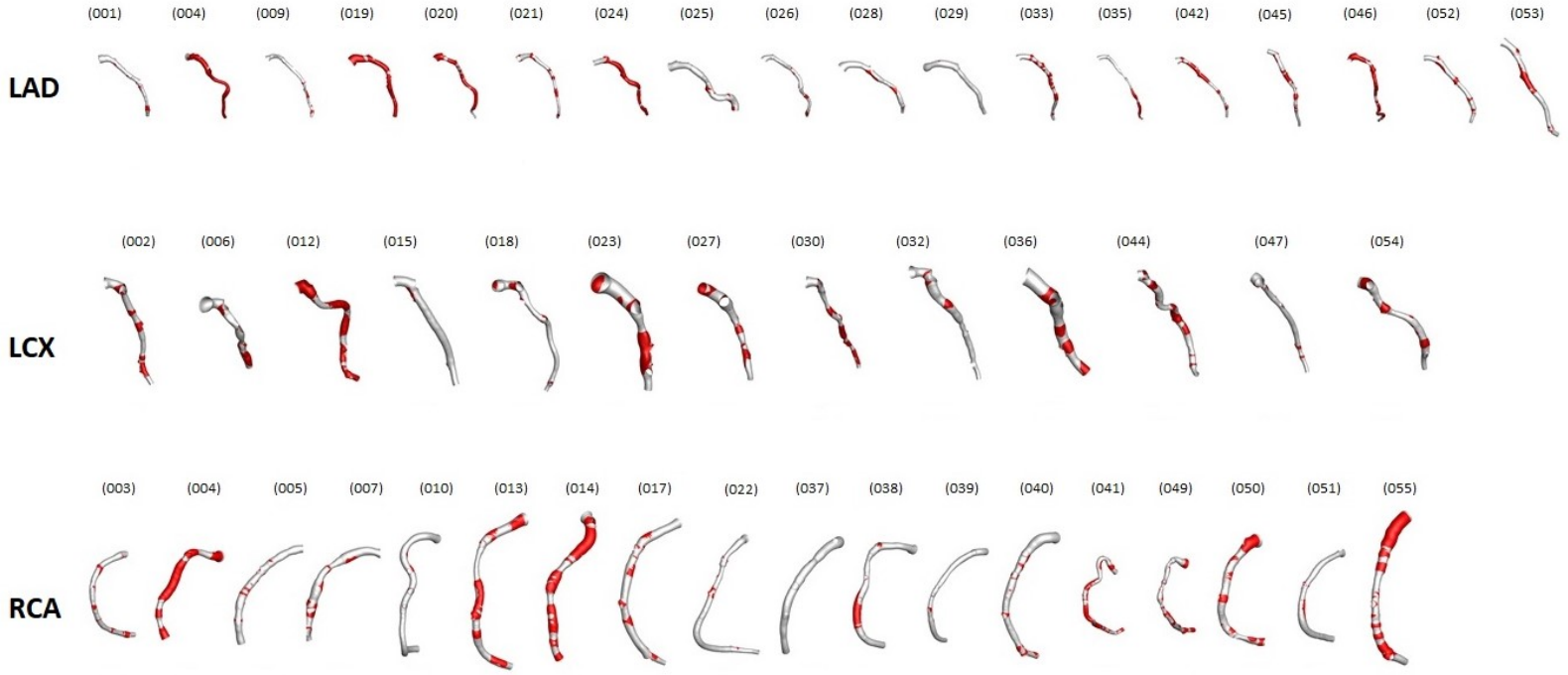

Figure 3.19: *Surface area of the 49 human artery models exposed to TAWSS33. Each one is identified by its identification number. Contour levels for TAWSS33 correspond to lowest tetrile value of TAWSS distribution on the combined surface of all models.*

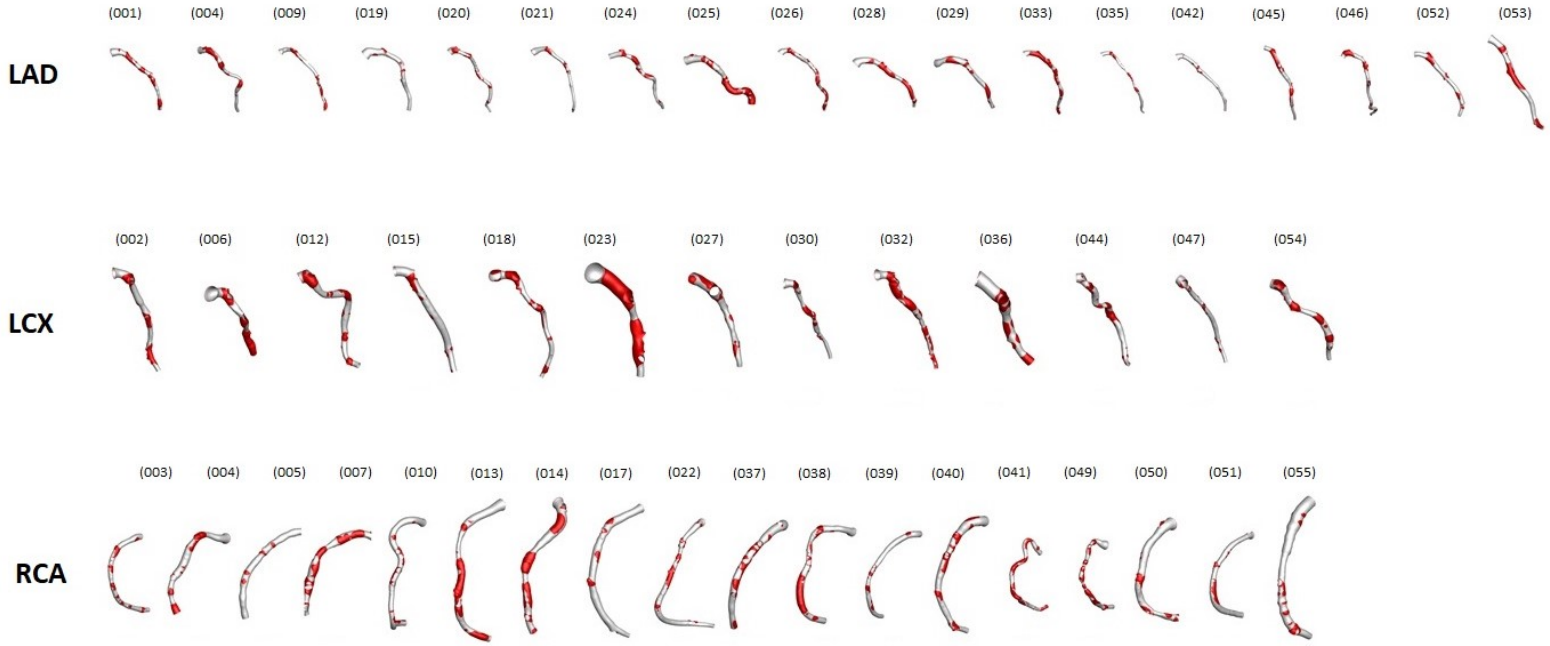

Figure 3.20: *Surface area of the 49 human artery models exposed to OSI66. Each one is identified by its identification number. Contour levels for OSI66 correspond to highest sixtile value of OSI distribution on the combined surface of all models.*

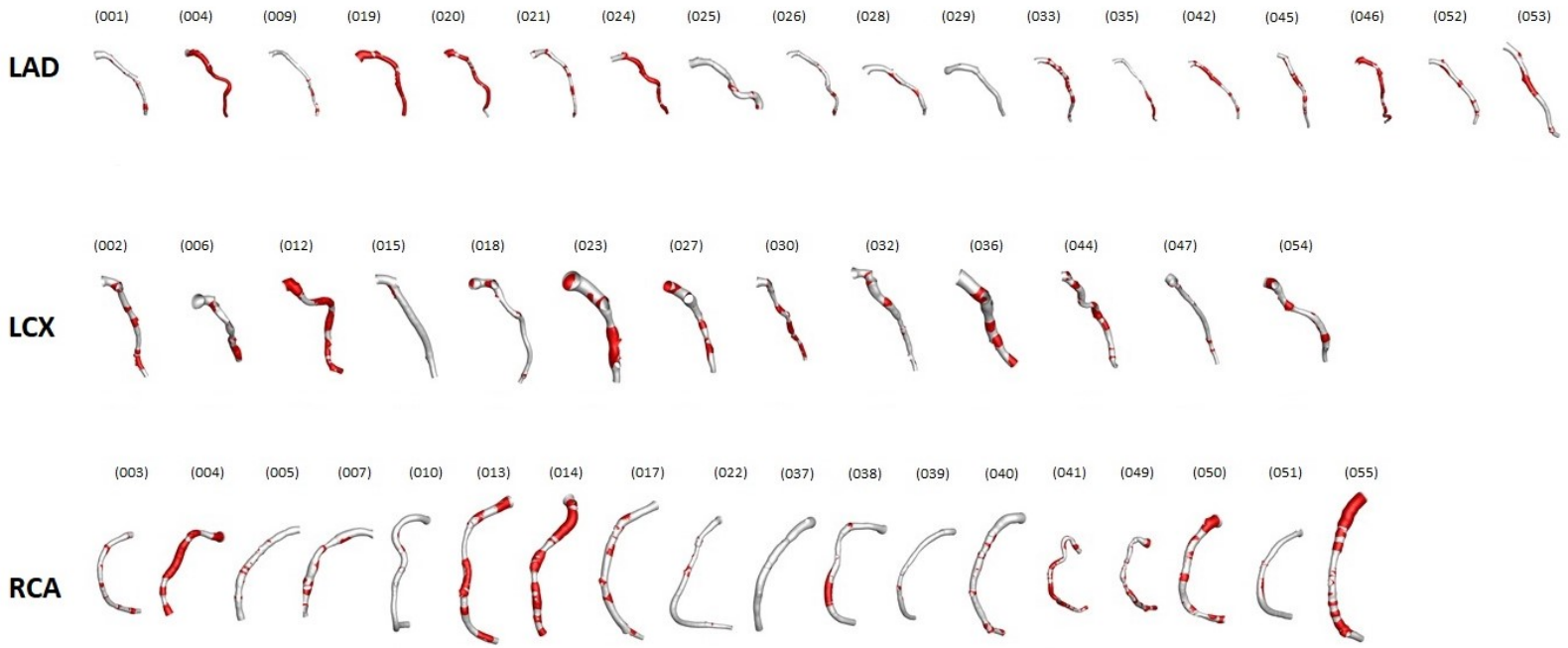

Figure 3.21: *Surface area of the 49 human artery models exposed to RRT66. Each one is identified by its identification number. Contour levels for RRT66 correspond to highest sixtile value of RRT distribution on the combined surface of all models.*

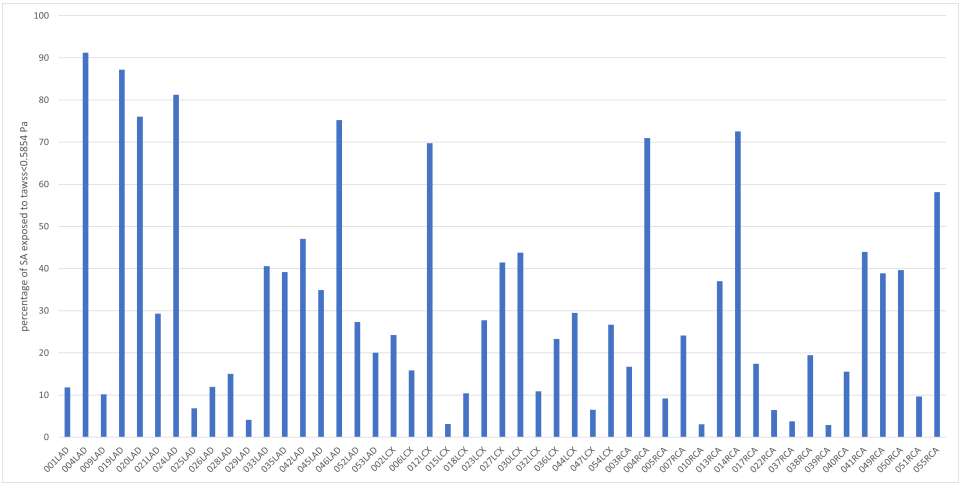

Figure 3.22: *Percentage of SA exposed to TAWSS < TAWSS33 for each coronary artery.*

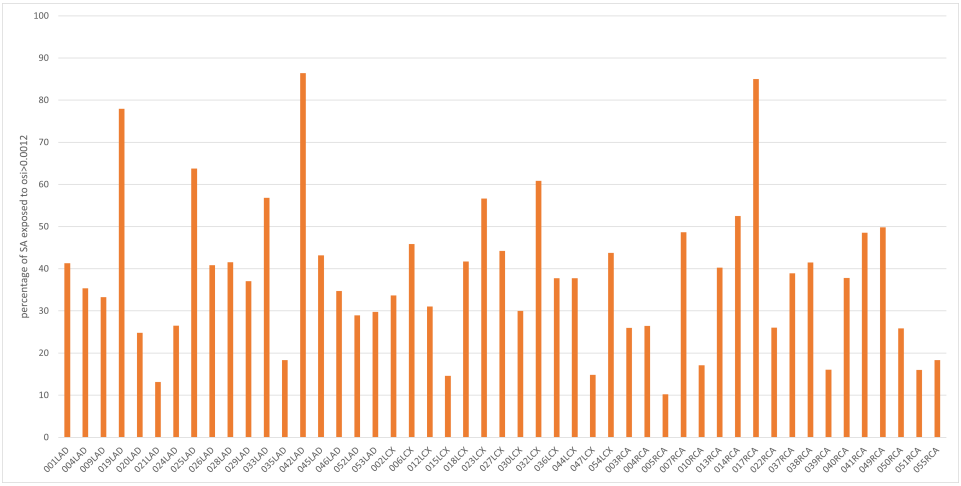

Figure 3.23: *Percentage of SA exposed to OSI > OSI66 for each coronary artery.*

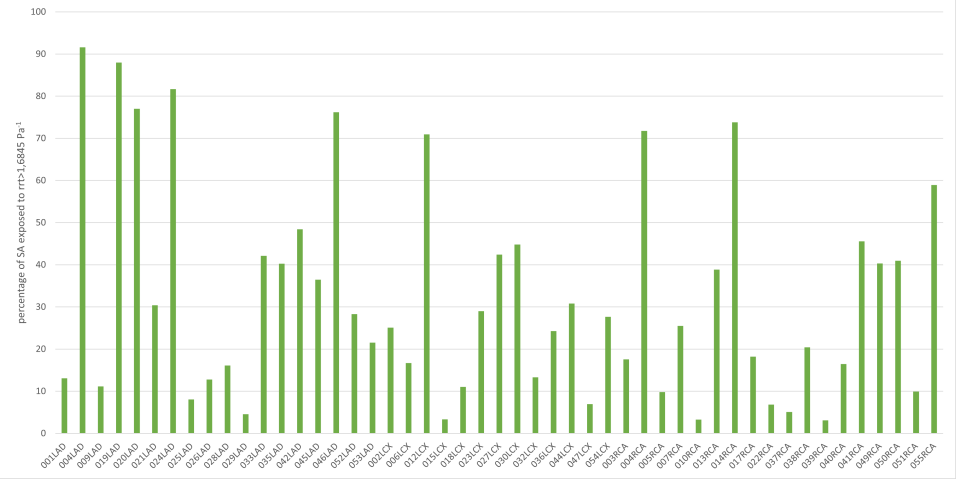

Figure 3.24: *Percentage of SA exposed to RRT > RRT66 for each coronary artery.*

Regression analysis reveal significant associations between the helicity-based parameter and the WSS-based descriptors [3] (Table 3.2). Among all the six descriptors, h_2 appears to be the one with the strongest association. In fact, it is strongly and negatively associated with the thresholds values of TAWSS and RRT ($r = -0.84$, $p < 0.001$), this means that the higher the h_2 is, the lower the SA of the artery is exposed to low WSS [3]. In contrast, with the other parameters there seems to be no association, this is because the correlation values are low and not very significant. It can also be noted that among all WSS-based descriptors, only %OSI66 presents positive correlation values and because of the fact that the threshold value is very low and non oscillatory (0.0012) in all the 49 models investigated, OSI is scarcely descriptive feature of the local hemodynamic.
Regarding geometric attributes, in Table 3.2 is shown that there isn't a correlation between helicity-based descriptors and curvature. In contrast, different information was emerged with the torsion. The findings revealed that exists a weak positive relationship with h_1 and moderate positive with h_3, thus suggesting a preferential direction of rotation of the bi-helical flow structures is promoted by vascular torsion..
In addition, it emerged that none of the volumetric descriptors (h_4 and h_5) have a statistical correlation with both WSS-based and vascular descriptors.

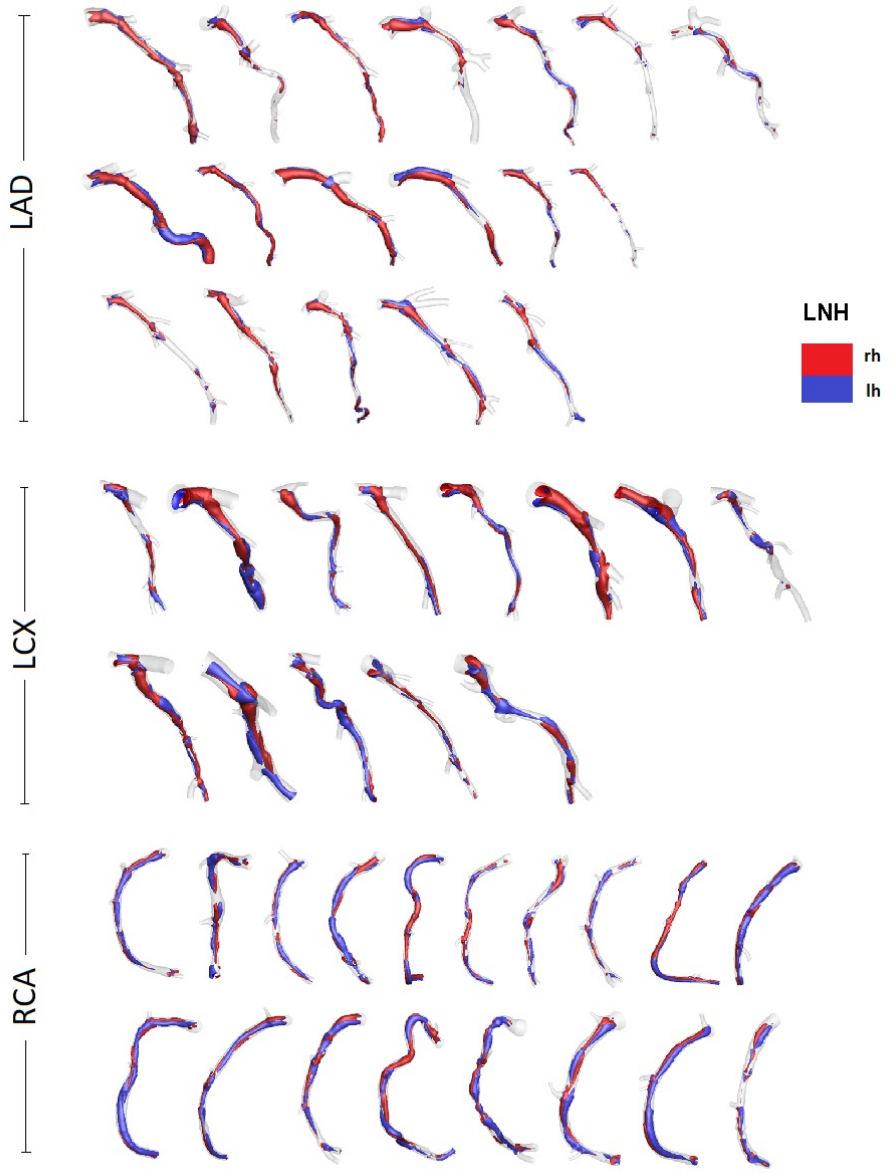

Figure 3.25: *Intravascular fluid structures in the 49 coronary arteries. Isosurfaces of cycle-average LNH (LNH = ± 0.2) are presented. Distinguishable left-handed (LNH < 0) and right-handed (LNH > 0) helical flow structures can be observed. They are sorted, from the top left to the bottom right, in ascending order of their identification number, respectively.*

Table 3.2: *Correlation coefficient for percentage luminal surface area exposed to disturbed shear and helicity-based descriptors and for hemodynamic descriptors vs average curvature and torsion.*

	h_1	h_2	h_3	h_4	h_5	h_6
%TAWSS33	- 0.26	**- 0.84**‡	- 0.14	- 0.12	- 0.14	- 0.12
%OSI66	0.1	0.07	0.19	0.14	0.23	0.14
%RRT66	- 0.26	**- 0.84**‡	-0.13	- 0.13	- 0.14	-0.12
$\bar{\kappa}$	- 0.23	- 0.16	- 0.24	0.05	0.13	0.05
$\bar{\tau}$	**0.32***	0.07	**0.39**†	0.26	0.15	0.26

Statistically significant values are in bold.
$^{*}p < 0.05$; $^{\dagger}p < 0.01$; $^{\ddagger}p < 0.001$.

The nature of the association between helicity-based descriptors and percentage of luminal SAs and geometry can be better appreciated in the following scatter plots, from Figure 3.26 to Figure 3.31. It emerges that exists a non-linear decreasing trend between h_2 and *%TAWSS33*, as well as for *%RRT66*, as expected because percentages of SA are almost identical (comparing Figure 3.22 to Figure 3.24); for the other parameters a non-relationship seems to exist.

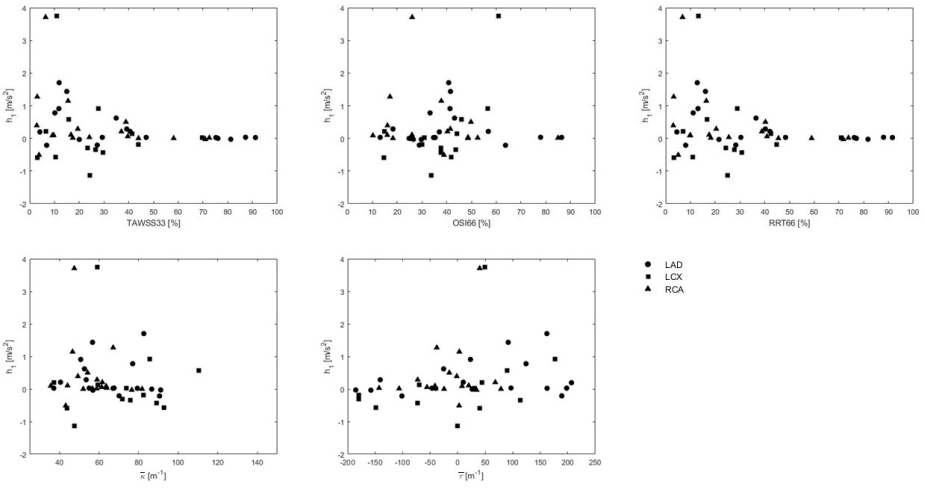

Figure 3.26: *Scatter plots of helicity intensity descriptors h_1 vs WSS-based descriptors and average curvature and torsion values.*

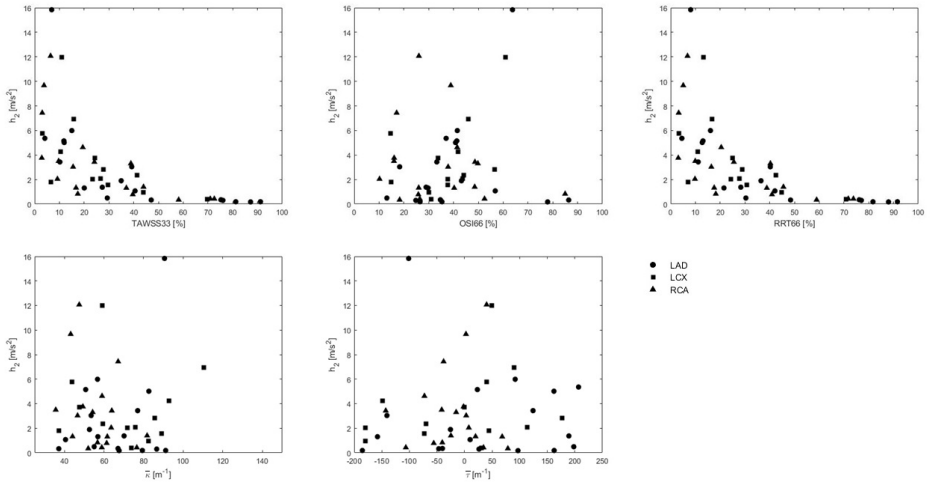

Figure 3.27: *Scatter plots of helicity intensity descriptors h_2 vs WSS-based descriptors and average curvature and torsion values.*

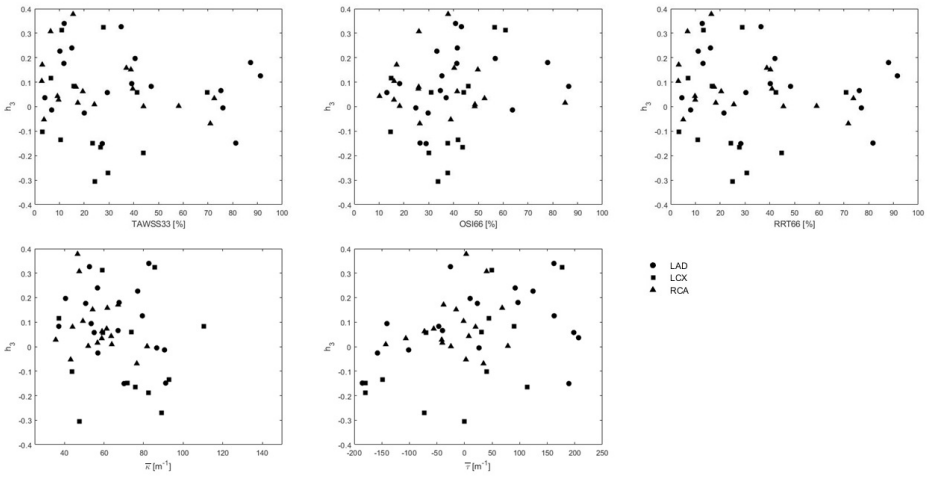

Figure 3.28: *Scatter plots of helicity intensity descriptors h_3 vs WSS-based descriptors and average curvature and torsion values.*

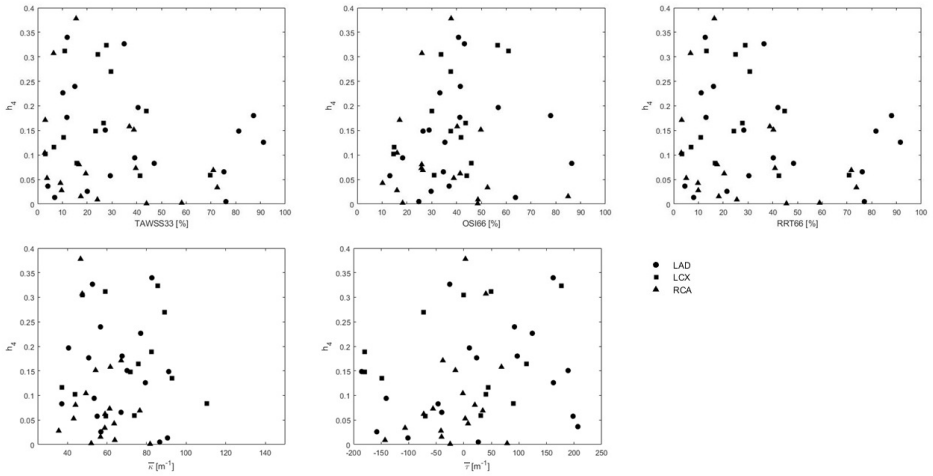

Figure 3.29: *Scatter plots of helicity intensity descriptors h_4 vs WSS-based descriptors and average curvature and torsion values.*

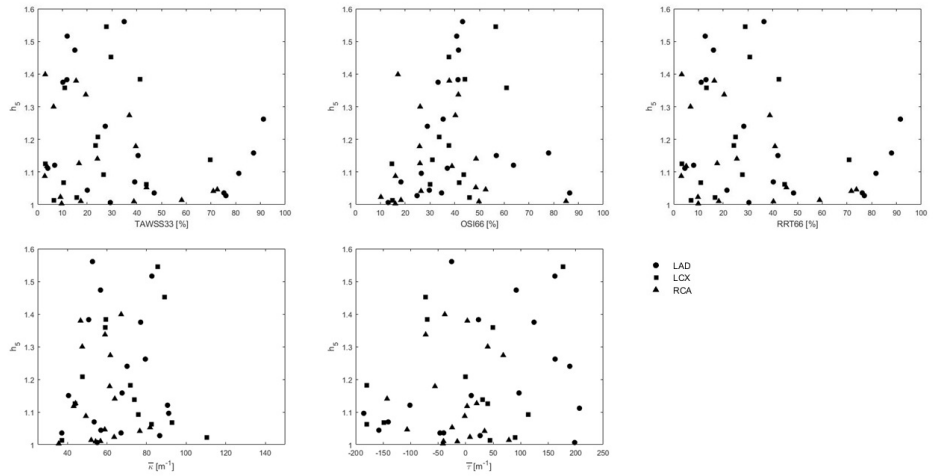

Figure 3.30: *Scatter plots of helicity intensity descriptors h_5 vs WSS-based descriptors and average curvature and torsion values.*

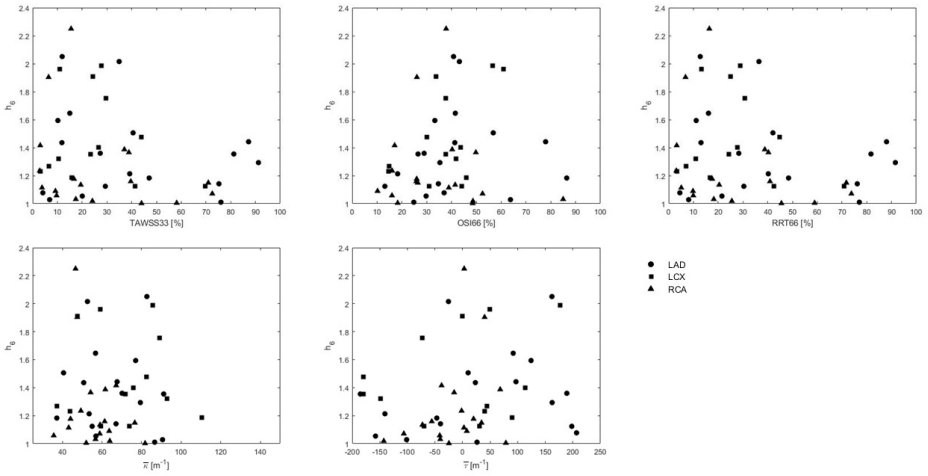

Figure 3.31: *Scatter plots of helicity intensity descriptors h_6 vs WSS-based descriptors and average curvature and torsion values.*

Chapter 4

DISCUSSION

The patient specific approach has been used mainly for small dataset in recent years, highlighting the existence of a link between helical flow and WSS in coronary arteries [27]. On the other hand, the majority of the already conducted researches on large dataset were done on computational models based on *in silico* experiments or with swine arteries. In this study the number of human coronary artery models evaluated is large and the measurements was done on patients, so the results are significant to support the existence of a link between helical flow, disturbed shear stress and vascular geometry.

As already seen in other report [3], here is confirmed that distinguishable counter-rotating helical flow patterns exists and they are in all the models investigated. This confirm that helical flow structures characterize the physiological intravascular hemodynamics in human coronary arteries. These structures stabilize the blood flow by lowering the WSS multidirectionality and minimizing the luminal surface exposed to low WSS when the average helicity intensity is high, which highlights the importance of helical flow in suppressing flow disturbance. Geometry influences by creating a preferential direction of rotation of the bi-helical flow structures is promoted by vascular torsion, while vascular curvature negatively affects the scarcely multidirectional WSS (Table 3.2)(adapted from [3]). In these cases, the very low values of OSI suggest a predominant role of low WSS in promoting endothelial dysfunction, as confirmed in other studies [5] [28], specifically as a determinant factor in plaque formation. Besides, in coronary arteries, volume variations appear to not be correlated to geometry and multidirectional WSS. To be honest, it is known that TAWSS and RRT promote shrinking of the vessel volume in the main flow direction, while the others a enlargement. Then, h_4 only gives information on the existence of a predominant

direction of the counter-rotating structures, without specifying their sign (information gives by h_3). Descriptor h_5 quantifies the volume occupied by arrangements in the dominant direction of rotation compared to the volume occupied by arrangement rotating in the opposite direction. In conclusion, both h_4 and h_5 give information on the presence of a dominant direction of rotation, rather then on the shrinking of the vessel.

However, these information does not reveal that a patient is more predisposed to vascular diseases than another one. The analysis of the SAs exposed to the threshold values can just suggest that the patient in question has an hemodynamic characterized by low values of TAWSS and lower flow rates on average.

Among all the assumptions we did, there are some that may limit the veridicity of the results. For instance the hypothesis of rigid walls, which may influence the valuation of TAWSS. However, there are actually a variety of studies that shows that the fluid structures are well approximated with the TAWSS distribution obtained [17].
In a patient specific computational fluid dynamics is important that every flow rate is associated with a specific geometry. These must be the effective flow rates in the patients. Therefore, the imposition of a generalized waveform could weaken the patient specific hypotesis. Actually, previous researches [12] confirm that these waveforms are absolutely comparable with the patient measured waveforms. Moreover, the cardiac-induced motion of coronary arteries was neglected. This idealization was based on previous findings demonstrating that myocardial motion has a minor effect on coronary flow and WSS distribution with respect to the blood pressure pulse [25] [29].

Future clinical perspective may involve the analysis of larger datasets for a better understanding of the pathophysiological mechanism leading to adverse vascular events or quantifying local wall thickness for the study of plaques growth in human specific computational models, for the ultimate prediction of the progression of atherosclerosis in coronaries.

In conclusion, this study confirms that hemodynamics in personalized computational models of human coronary arteries is characterized by counter-rotating bi-helical flow structures, whose topological features are associated with geometry (dependant on average torsion). In addition, it emerges that unfavorable conditions of low WSS are strongly and inversely associated with helicity intensity, as already studied in other arterial districts [6], while the volumetric helicity descriptors did not show any relationship with multidirectional WSS.

Bibliography

[1] Jordi Alastruey, Jennifer H Siggers, Véronique Peiffer, Denis J Doorly, and Spencer J Sherwin. Reducing the data: Analysis of the role of vascular geometry on blood flow patterns in curved vessels. *Physics of Fluids*, 24(3):031902, 2012.

[2] Giuseppe De Nisco, Ayla Hoogendoorn, Claudio Chiastra, Diego Gallo, Annette M Kok, Umberto Morbiducci, and Jolanda J Wentzel. The impact of helical flow on coronary atherosclerotic plaque development. *Atherosclerosis*, 2020.

[3] Giuseppe De Nisco, Annette M Kok, Claudio Chiastra, Diego Gallo, Ayla Hoogendoorn, Francesco Migliavacca, Jolanda J Wentzel, and Umberto Morbiducci. The atheroprotective nature of helical flow in coronary arteries. *Annals of biomedical engineering*, 47(2):425–438, 2019.

[4] Lee J Frazin, Gregory Lanza, Michael Vonesh, Fouad Khasho, Caryn Spitzzeri, Sandra McGee, David Mehlman, KB Chandran, James Talano, and David McPherson. Functional chiral asymmetry in descending thoracic aorta. *Circulation*, 82(6):1985–1994, 1990.

[5] Diego Gallo, Payam B Bijari, Umberto Morbiducci, Ye Qiao, Yuanyuan Xie, Maryam Etesami, Damiaan Habets, Edward G Lakatta, Bruce A Wasserman, and David A Steinman. Segment-specific associations between local haemodynamic and imaging markers of early atherosclerosis at the carotid artery: an in vivo human study. *Journal of The Royal Society Interface*, 15(147):20180352, 2018.

[6] Diego Gallo, David A Steinman, Payam B Bijari, and Umberto Morbiducci. Helical flow in carotid bifurcation as surrogate marker of exposure to disturbed shear. *Journal of biomechanics*, 45(14):2398–2404, 2012.

[7] Eline MJ Hartman, Giuseppe De Nisco, Annette M Kok, Ayla Hoogendoorn, Adriaan Coenen, Frits Mastik, Suze-Anne Korteland, Koen Nieman, Frank JH Gijsen, Anton FW van der Steen, et al. Lipid-rich plaques detected by near-infrared spectroscopy are more frequently exposed to high shear stress. *Journal of Cardiovascular Translational Research*, pages 1–10, 2020.

[8] Heather A Himburg, Deborah M Grzybowski, Andrew L Hazel, Jeffrey A LaMack, Xue-Mei Li, and Morton H Friedman. Spatial comparison between wall shear stress measures and porcine arterial endothelial permeability. *American Journal of Physiology-Heart and Circulatory Physiology*, 286(5):H1916–H1922, 2004.

[9] Ayla Hoogendoorn, Annette M Kok, Eline MJ Hartman, Giuseppe de Nisco, Lorena Casadonte, Claudio Chiastra, Adriaan Coenen, Suze-Anne Korteland, Kim Van der Heiden, Frank JH Gijsen, et al. Multidirectional wall shear stress promotes advanced coronary plaque development: comparing five shear stress metrics. *Cardiovascular Research*, 116(6):1136–1146, 2020.

[10] J Graeme Houston, Stephen J Gandy, Wendy Milne, John BC Dick, Jill JF Belch, and Peter A Stonebridge. Spiral laminar flow in the abdominal aorta: a predictor of renal impairment deterioration in patients with renal artery stenosis? *Nephrology Dialysis Transplantation*, 19(7):1786–1791, 2004.

[11] J Graeme Houston, Stephen J Gandy, Declan G Sheppard, John B Dick, Jill JF Belch, and Peter A Stonebridge. Two-dimensional flow quantitative mri of aortic arch blood flow patterns: Effect of age, sex, and presence of carotid atheromatous disease on prevalence of spiral blood flow. *Journal of Magnetic Resonance Imaging: An Official Journal of the International Society for Magnetic Resonance in Medicine*, 18(2):169–174, 2003.

[12] Yunlong Huo and Ghassan S Kassab. Intraspecific scaling laws of vascular trees. *Journal of The Royal Society Interface*, 9(66):190–200, 2012.

[13] MR Kaazempur-Mofrad and CR Ethier. Mass transport in an anatomically realistic human right coronary artery. *Annals of Biomedical Engineering*, 29(2):121–127, 2001.

[14] Philip J Kilner, Guang Z Yang, Raad H Mohiaddin, David N Firmin, and Donald B Longmore. Helical and retrograde secondary flow pat-

terns in the aortic arch studied by three-directional magnetic resonance velocity mapping. *Circulation*, 88(5):2235–2247, 1993.

[15] DN Ku, DP Giddens, DJ Phillips, and DE Strandness Jr. Hemodynamics of the normal human carotid bifurcation: in vitro and in vivo studies. *Ultrasound in medicine & biology*, 11(1):13–26, 1985.

[16] Xiao Liu, Yubo Fan, X Yun Xu, and Xiaoyan Deng. Nitric oxide transport in an axisymmetric stenosis. *Journal of the Royal Society Interface*, 9(75):2468–2478, 2012.

[17] M Malvè, A García, J Ohayon, and MA Martínez. Unsteady blood flow and mass transfer of a human left coronary artery bifurcation: Fsi vs. cfd. *International communications in heat and mass transfer*, 39(6):745–751, 2012.

[18] Colin D Mathers and Dejan Loncar. Projections of global mortality and burden of disease from 2002 to 2030. *PLoS medicine*, 3(11):e442, 2006.

[19] Umberto Morbiducci, Raffaele Ponzini, Mauro Grigioni, and Alberto Redaelli. Helical flow as fluid dynamic signature for atherogenesis risk in aortocoronary bypass. a numeric study. *Journal of biomechanics*, 40(3):519–534, 2007.

[20] Umberto Morbiducci, Raffaele Ponzini, Giovanna Rizzo, Marcello Cadioli, Antonio Esposito, Franco Maria Montevecchi, and Alberto Redaelli. Mechanistic insight into the physiological relevance of helical blood flow in the human aorta: an in vivo study. *Biomechanics and modeling in mechanobiology*, 10(3):339–355, 2011.

[21] Warwick S Nesbitt, Erik Westein, Francisco Javier Tovar-Lopez, Elham Tolouei, Arnan Mitchell, Jia Fu, Josie Carberry, Andreas Fouras, and Shaun P Jackson. A shear gradient–dependent platelet aggregation mechanism drives thrombus formation. *Nature medicine*, 15(6):665–673, 2009.

[22] Laura M Sangalli, Piercesare Secchi, Simone Vantini, and Alessandro Veneziani. Efficient estimation of three-dimensional curves and their derivatives by free-knot regression splines, applied to the analysis of inner carotid artery centrelines. *Journal of the Royal Statistical Society: Series C (Applied Statistics)*, 58(3):285–306, 2009.

[23] Michiel Schaap, Lisan Neefjes, Coert Metz, Alina van der Giessen, Annick Weustink, Nico Mollet, Jolanda Wentzel, Theo van Walsum, and Wiro Niessen. Coronary lumen segmentation using graph cuts and robust kernel regression. In *International Conference on Information Processing in Medical Imaging*, pages 528–539. Springer, 2009.

[24] PA Stonebridge and CM Brophy. Spiral laminar flow in arteries? *The Lancet*, 338(8779):1360–1361, 1991.

[25] PA Stonebridge, SA Suttie, R Ross, and J Dick. Spiral laminar flow: a survey of a three-dimensional arterial flow pattern in a group of volunteers. *European Journal of Vascular and Endovascular Surgery*, 52(5):674–680, 2016.

[26] Glenn Van Langenhove, JJ Wentzel, Rob Krams, CJ Slager, JN Hamburger, and PW Serruys. Helical velocity patterns in a human coronary artery: a three-dimensional computational fluid dynamic reconstruction showing the relation with local wall thickness. *Circulation*, 102(3):e22–e24, 2000.

[27] Natalya Vorobtsova, Claudio Chiastra, Mark A Stremler, David C Sane, Francesco Migliavacca, and Pavlos Vlachos. Effects of vessel tortuosity on coronary hemodynamics: an idealized and patient-specific computational study. *Annals of biomedical engineering*, 44(7):2228–2239, 2016.

[28] Jolanda J Wentzel, Yiannis S Chatzizisis, Frank JH Gijsen, George D Giannoglou, Charles L Feldman, and Peter H Stone. Endothelial shear stress in the evolution of coronary atherosclerotic plaque and vascular remodelling: current understanding and remaining questions. *Cardiovascular research*, 96(2):234–243, 2012.

[29] Dehong Zeng, Zhaohua Ding, Morton H Friedman, and C Ross Ethier. Effects of cardiac motion on right coronary artery hemodynamics. *Annals of biomedical engineering*, 31(4):420–429, 2003.